1 **Initiation phase cellular reprogramming ameliorates DNA damage in the ERCC1 mouse**
2 **model of premature aging.**
3
4 Patrick Treat Paine[1], Cheyenne Rechsteiner[2], Francesco Morandini[2], Gabriela Desdin Mico[1],
5 Calida Mrabti[1], Alberto Parras[1], Amin Haghani[3], Robert Brooke[4], Steve Horvath[3,4,5], Andrei
6 Seluanov[2], Vera Gorbunova[2], Alejandro Ocampo[1]
7
8 [1]Department of Biomedical Sciences, Faculty of Biology and Medicine, University of Lausanne,
9 Lausanne, Vaud, Switzerland.
10 [2]Departments of Biology and Medicine, University of Rochester, Rochester, NY, USA
11 [3] Altos Labs, San Diego, USA
12 [4] Epigenetic Clock Development Foundation, Torrance, CA, USA
13 [5] Human Genetics, David Geffen School of Medicine, University of California, Los Angeles, USA
14
15 **Correspondence:** alejandro.ocampo@unil.ch
16
17 **Keywords:** progeria, DNA damage, ERCC1, accelerated aging, cellular reprogramming, TGFb
18
19
20
21
22
23
24
25
26
27
28
29
30
31
32
33
34
35
36
37
38

Abstract

40 Unlike aged somatic cells, which exhibit a decline in molecular fidelity and eventually reach a state
41 of replicative senescence, pluripotent stem cells can indefinitely replenish themselves while
42 retaining full homeostatic capacity. The conferment of beneficial-pluripotency related traits via in
43 vivo partial cellular reprogramming (IVPR) significantly extends lifespan and restores aging
44 phenotypes in mouse models. Although the phases of cellular reprogramming are well
45 characterized, details of the rejuvenation processes are poorly defined. To understand whether
46 epigenetic reprogramming can ameliorate DNA damage, we created reprogrammable accelerated
47 aging mouse model with an ERCC1 mutation. Importantly, using enhanced partial reprogramming
48 by combining small molecules with the Yamanaka factors, we observed potent reversion of DNA
49 damage, significant upregulation of multiple DNA damage repair processes, and restoration of the
50 epigenetic clock. In addition, we present evidence that pharmacological inhibition of ALK5 and
51 ALK2 receptors in TGFb pathway is able to phenocopy some benefits including epigenetic clock
52 restoration suggesting a role in the mechanism of rejuvenation by partial reprogramming.

Introduction

55 The phenomenon of aging is directly linked to a decline in cellular repair functions with an
56 associated increase in aging phenotypes including genomic instability[1–3]. DNA damage events due
57 to radiation, reactive oxygen species, chemicals, or replication errors can overwhelm DNA repair
58 functions and are proposed as a causative factor for epigenetic dysregulation and a key contributor
59 to age associated pathologies[4–8]. In this line, Ercc1$^{\Delta/-}$ progeroid mice, harboring a single truncated
60 Ercc1 allele required for nucleotide excision repair (NER), interstrand crosslink repair (ICL), and
61 homologous repair (HR) display increased DNA damage and a broad spectrum of aging
62 phenotypes including senescence, neurodegeneration, multi-morbidity, and a shortened lifespan[9–
63 13]. Interestingly, a recent comparative lifespan analysis of 18 wildtype rodent species indicates
64 DNA double-strand break repair was more efficient in long-lived species[14]. For these reasons, DNA
65 repair mutant Ercc1$^{\Delta/-}$ mice are an ideal alternative for investigating aging interventions and DNA
66 repair-related mechanisms of rejuvenation in particular[9,15,16].

68 Cellular reprogramming can be defined as the conversion of a somatic cell to pluripotency and can
69 be induced via the forced expression of four defined transcription factors; Oct4, Sox2, Klf4, and c-
70 Myc (OSKM)[17]. The resulting induced pluripotent stem cells (iPSCs) exhibit a dedifferentiated cell
71 identity similar to embryonic stem cells (ESCs) along with a restoration of aged phenotypes[18,19].
72 Recently, in vivo partial reprogramming (IVPR), following short-term cyclic expression of OSKM,
73 has emerged as a novel therapeutic strategy for the treatment of age-related diseases (ARDs)[20–
74 22]. Specifically, partial cellular reprogramming has produced improvements to lifespan, hallmarks
75 of aging, the epigenetic clock, and tissue regeneration in progeroid and wildtype mouse models in
76 vivo[6,23–34]. Multiple in vitro time course studies have demonstrated reprogramming initially

77 proceeds in a multifactorial manner involving extensive epigenetic remodeling, cell cycle induction

78 with a shorted G1 phase, mesenchymal to epithelial transition due to TGFb inhibition, and BMP

79 induction, while undergoing a major reset to the proteome and transcriptome[35–45]. Importantly, in

80 what manner and to what extent these early alterations to molecular and cellular processes via

81 IVPR counter and reverse aging drivers is currently unknown.

82

83 To address this limitation and gain a deeper understanding of the mechanisms involved in age

84 amelioration by OSKM induction, we have chosen to investigate the effects of partial

85 reprogramming in the Ercc1$^{\Delta/-}$ DNA damage model of accelerated aging. Using an in vitro time

86 course capable of dissecting time dependent processes, we characterized the early events of

87 reprogramming in a novel reprogrammable Ercc1$^{\Delta/-}$ accelerated aging mouse model. Most

88 importantly, we observed a significant reduction in DNA damage beginning at 2 days of

89 reprogramming demonstrating reversal of a key hallmark of aging. At the same time RNA seq

90 analysis shows a significant upregulation of nearly every major DNA repair pathway while DNA

91 methylation clock analysis shows a reversal of epigenetic age. Interestingly, improvements were

92 more robust in the Ercc1 DNA damage model versus the wildtype cells, as would be expected from

93 an improvement to homeostatic capacity. Lastly, small molecule inhibition of the TGFb pathway

94 was sufficient to phenocopy some rejuvenating aspects of reprogramming including a decrease in

95 nuclear size, decreased yH2AX, and restoration of the epigenetic clock.

96

97 **Results**

98 **Induced reprogramming in a mouse model of accelerated aging decreases DNA damage**

99 OSKM-mediated partial cellular reprogramming has been shown to mitigate genomic instability

100 and epigenetic alterations in wildtype and Lamin A mutant mouse fibroblasts as well as in vitro

101 aged nucleus pulposus cells[23,31]. On other hand, it is currently unknown whether this restoration

102 would occur in an Ercc1 DNA damage model of accelerated aging with defects in DNA repair. To

103 address this question, we developed a novel doxycycline-inducible mouse model of

104 reprogrammable aging (Ercc1$^{\Delta/-}$ 4Fj$^{+/-}$ rtTA$^{+/-}$) containing a single truncated Ercc1 allele, Col1a1-

105 tetO-OSKM polycistronic transgene, and the ROSA26-M2-rtTA allele (Fig. 1a).

106

107 To first verify the presence of DNA damage in our reprogrammable progeria model, adult tail tip

108 fibroblasts (FBs) were isolated from the 4Fj Ercc1$^{\Delta/-}$ (D/KO) and 4Fj Ercc1$^{+/+}$ (WT) mice, stained

109 for the DNA damage marker γH2AX, and imaged with confocal laser microscopy. As expected, a

110 significant increase in yH2AX fluorescence was observed in the D/KO fibroblasts compared to the

111 WT (Fig. 1c, s1a). In addition, this accelerated aging cell model also displayed a significant

112 increase in nuclear area in these samples, based on nuclear staining with DAPI (Fig. S1b). This

113 experiment confirmed the presence of a DNA repair defect in our novel OSKM inducible mouse

114 model of aging along with an enlarged nucleus compared to WT (Fig. S1a,b).

115

116   In vitro cellular reprogramming time course experiments have previously been used to identify
117   three phases of reprogramming including initiation, maturation, and stabilization[46,47]. Initiation
118   phase proceeds via alterations to several key biological processes including proliferation,
119   chromatin modification, DNA damage repair, mesenchymal to epithelial transition (MET), and RNA
120   processing[33,41–45,48–50]. To gain insight into partial reprogramming processes with the capacity to
121   restore homeostatic function in a DNA damage model, a time course analysis of the initiation phase
122   of reprogramming was performed (Fig. 1b). At the same time, the induction of pluripotency in
123   somatic cells following OSKM expression is a stochastic, asynchronous, and inefficient process
124   often taking weeks with a low percentage of iPSC colonies[51,52]. To facilitate an accelerated
125   reprogramming process and enhance the ability to delineate reprogramming-induced aging
126   phenotypes in bulk cultures a previously identified small molecule combination, Vitamin C (V) and
127   CHIR-99021 (C), was selected[53–55]. Alone, Vitamin C is able lower the epigenetic barrier of
128   pluripotent gene expression due to its function as a histone demethylase and Tet enzyme cofactor
129   while CHIR activates the Wnt pathway and promotes glycolysis via GSK3-beta inhibition[56–58].

130

131   To confirm the induction of cellular reprogramming following expression of OSKM in our
132   reprogrammable DNA damage model, doxycycline (2ug/mL) was added to 4F Ercc1 cells in culture
133   alone or combined with VC and imaged with brightfield microscopy at 4x during days 0 – 4 (Fig.
134   1a,b). A clear shift in cell morphology with a cobblestone appearance associated with MET is
135   present after 2 days, more so after 4 days, and most strongly in the enhanced D4+VC group (Fig.
136   1e). Expression of the Klf4 and Sox2 transcription factors were observed only after doxycycline
137   induction and most strongly at d4+VC but never day 0 based on immunofluorescence (IF) laser
138   confocal imaging (Fig. 1d, S1c). These cells retained the fibroblast identity marker Thy1.2 at D4
139   with or without VC, as shown by flow cytometry, indicating this mouse model and experimental
140   setup successfully represent initiation phase partial reprogramming without dedifferentiation or
141   entrance into a pluripotent state (Fig. 1g, s1d).

142

143   In regards to the effects of cellular reprogramming on yH2AX in this DNA damage model, we first
144   used flow cytometry. Specifically, two days of doxycycline induced reprogramming in the D/KO
145   was sufficient to decrease median yH2AX fluorescent intensity per cell by 38% (Fig. S1e). Next,
146   using IF and confocal imaging, we observed a significant decrease in mean yH2AX level per cell
147   after 2 and 4 days of reprogramming (Fig. 1g, h, S1j). Similarly, enhanced reprogramming with VC
148   also restored this DNA damage marker significantly after 2 and 4 days of OSKM induction (Fig.
149   1g, h, S1j). These D/KO cells also displayed a significant reduction in nuclear size during
150   reprogramming after induction with doxycycline for 2 or 4 days (Fig. 1i). When this experiment was
151   repeated on OSKM inducible WT cells without the DNA repair defect, it also showed a significant
152   decrease in yH2AX signal and decrease in nuclear area (Fig. S1f). Thus, initiation phase cellular

153   reprogramming is sufficient to ameliorate a key driver of aging even in mutant cells defective for

154   DNA repair responsible for NER, ICL, and HR.

155

156   **The DNA methylation clock is restored in Ercc1$^{\Delta/-}$ following short term reprogramming**

157   Recent evidence from our lab indicates that D/KO FBs display accelerated aging based on the

158   DNA methylation clock and are therefore a good *in vitro* model to investigate aging mechanisms

159   and interventions[59]. Furthermore, cellular reprogramming has been observed to reverse epigenetic

160   age in mouse and human cell types but the effects on an accelerated aging model with a DNA

161   repair defect are unknown[60,61]. In order to investigate the effect of reprogramming on the DNA

162   methylation clock, we applied the DNA Methyl Age Skin Final clock to all samples and timepoints.

163   Strikingly, enhanced reprogramming with VC for 4 days in the D/KO produced a significant

164   restoration to the DNA methylation clock with the top responder showing a 54% decrease in

165   epigenetic age (Fig. 2a). At the same time, there was a trend towards epigenetic clock restoration

166   after 2 and 4 days of reprogramming although not significant, perhaps due to less efficient

167   reprogramming (Fig. 2a). Significant restoration to the DNAm clock only occurred at day 2 in WT

168   FBs (Fig. s2a). In addition, variability was greater in the WT samples perhaps due to the stochastic

169   nature of reprogramming and the early time point chosen for analysis, or the lack of accelerate

170   aging phenotype (Fig. s2a). The robust reversal of the DNAm clock in the D/KO FBs indicates

171   enhanced reprogramming is capable of cellular rejuvenation in an aging model with defective DNA

172   repair.

173

174   Next, as chromatin remodeling and reversal of the DNA methylation clock are observed to coincide

175   during cellular reprogramming, we sought to understand the epigenetic alterations that occur

176   following reprogramming in this Ercc1 model[48,61]. First, a significant increase in H3K9me3 was

177   observed in the D/KO fibroblasts compared to WT controls based on IF confocal imaging at 100x

178   (Fig. 2b, s2b). A similar increase was observed in the heterochromatin mark H4K20me3 while

179   H3K27me3 remained unchanged under the same conditions (Fig. s2d, e). These results were then

180   confirmed with western capillary analysis (Fig s2c). We hypothesize that this *in vitro* phenotype of

181   chromatin compaction is an adaptation in these cells to protect against chronic elevated DNA

182   damage levels[62,63]. Interestingly, when reprogramming or enhanced reprogramming was induced

183   for 2 or 4 days, heterochromatin was significantly decreased in this DNA damage model shifting it

184   towards wildtype levels (Fig. 2c, d, e, s2g, h, I, and j). This restoration of heterochromatin levels in

185   D/KO FBs coincides with improvement to reversion of the DNAm clock, in line with previous reports

186   suggesting a mechanistic relationship[6,23,32].

187

188   **Homeostatic capacity is significantly upregulated during the initiation phase of cellular**

189   **reprogramming**

5

190   To better understand the effects of reprogramming in this DNA damage model, paired-end bulk
191   RNA sequencing and analysis was performed for each treatment and time point. Principal
192   component analysis (PCA) based on relative gene expression values confirmed groups clustered
193   based on the treatment, timepoint, and cell type while displaying a reprogramming trajectory from
194   day 0 to day 4 (Fig. 3a). Interestingly, the enhanced reprogramming at day 2 plus VC was equal
195   to 4 days of reprogramming alone based on overlapping PCA scores (Fig. 3a). At the same time,
196   D/KO cells displayed a larger shift in PC2 score than WT following reprogramming (Fig. 3a). Venn
197   diagrams and associated gene expression heat maps were created based on the normalized
198   transcriptomes from each group and demonstrate a shared gene profile during reprogramming
199   albeit with some unique differences (Fig. 3b, 3c). In particular, over 1400 genes were uniquely
200   upregulated and 992 downregulated in the D/KO Fbs during initiation phase with enhanced
201   reprogramming compared to reprogrammed WT cells (Fig. 3c). The most robust changes were
202   observed following enhanced reprogramming to the D/KO group, indicating a profound and rapid
203   reset to the transcriptome in this DNA damage model (Fig. 3b, 3c). GO term analysis demonstrated
204   a significant upregulation of DNA damage repair pathways in the D/KO enhanced reprogramming
205   group including DNA repair, homologous recombination (HR), non-homologous end joining
206   (NHEJ), base excision repair (BER), mismatch repair (MMR), nucleotide excision repair (NER),
207   and alternative end joining (AltEJ), while interstrand crosslink repair (ICR) showed a trend towards
208   upregulation. (Fig. 3d, S3a). At the same time, reprogramming in WT cells did not produce such
209   broad and robust effects on DNA repair processes (Fig. 3d, S3a). Other notable processes
210   increased with enhanced reprogramming include chromatin organization pathways in D/KO cells
211   (Fig. 3d, S3a). Importantly, there was also a significant downregulation in TGFb receptor signaling
212   and TGFb regulation pathways as well as a decrease in EMT pathways (Fig. 3d, S3a). Gene set
213   enrichment analysis (GSEA) showed that intermediate filament cytoskeleton organization and
214   processes, keratinocyte differentiation and epidermal differentiation were significantly upregulated
215   at all timepoints and models (Fig. S3b). At the same time, Reactome analysis showed that
216   Keratinization and Formation of the Cornified Envelope were also universally upregulated (Fig.
217   S3c). Together, this transcriptomic data provides a mechanistic basis that supports the observed
218   changes to morphological, epigenetic, and DNA damage phenotypes that occur following short-
219   term reprogramming in our DNA damage model. Interestingly, the robust upregulation of major
220   DNA repair processes in the Ercc1 model vs WT suggest a homeostatic process capable of
221   responding to intrinsic molecular and age-related defects that characterized Ercc1 cells.
222

223   **TGFb inhibition alone improves DNA damage phenotypes and rejuvenates the DNA**
224   **methylation clock**
225   The RNA seq analysis showing downregulation of TGFb signaling and associated epithelial to
226   mesenchymal transition pathways is a well-documented early event of cellular reprogramming
227   following OSKM induction[35,40,41,64]. In contrast, upregulation of TGFb signaling is a driver of aging

6

228   phenotypes including cell degeneration, fibrosis, ROS, inflammation, DNA damage, senescence,
229   and stem cell aging[65–68]. Recently our lab observed that inhibition of the TGFb pathway is able to
230   extend lifespan in C. elegans, supporting its role in aging and longevity[69]. Based on these
231   observations, we asked whether TGFb inhibition alone could impact DNA damage and the DNA
232   methylation clock in our Ercc1 accelerated aging model in a manner similar to reprogramming (Fig.
233   3a). In this line, the TGFb superfamily consists of over 30 subtypes but for this study we focused
234   on canonical TGFb signaling and the bone morphogenic protein pathway (BMP) as both have been
235   identified to be important for early stage reprogramming [41,53,70]. Specifically, 9 inhibitors that target
236   the TGFb ALK5 receptor and 6 inhibitors that target the BMP ALK2 receptors were screened for 3
237   days on D/KO fibroblasts. Following a cell viability study to confirm a safe dosage range, a high or
238   low dose of each inhibitor was added to the Ercc1 fibroblasts for 3 days and analyzed for changes
239   to yH2AX using IF and confocal microscopy (Fig. S4a). Surprisingly, all of the ALK5 inhibitors
240   successfully decreased yH2AX levels based on IF, although in some cases it was dose-dependent
241   (Fig. 4b). Similarly, all but one of the ALK2 inhibitors also decreased DNA damage in Ercc1
242   fibroblasts, although not as effectively as the ALK5 inhibitors, again in a dose dependent manner
243   (Fig. 4c). Subsequently, we repeated these experiments with only the top performers including
244   ALK5 inhibitors Repsox and A83-01, ALK2 inhibitor DMH-1, and dual ALK5 and ALK2 inhibitor
245   Vactosertib. Once again, each of the inhibitors decreased the yH2AX signal of Ercc1 fibroblasts
246   below control levels although the ALK2 inhibitor, DMH-1, was less effective than the three ALK5
247   inhibitors (Fig. s4b). Interestingly, when nuclear area was calculated based on DAPI staining,
248   DMH-1 was also the only inhibitor not to show a trend towards decreased nuclear size potentially
249   implying an association between nuclear size changes and improvements in DNA repair (Fig. s4).
250   In contrast, other small molecules previously shown to induce pluripotency when applied as a
251   cocktail were unable to decrease yH2AX levels in Ercc1 fibroblasts when applied individually
252   including valproic acid (VPA), CHIR, tranylcypromine (TCP), Forskolin, DZNep, or TTNPB (Fig.
253   s4c) [71,72]. When the ALK5 inhibitor, Repsox, was combined with 4 days of reprogramming, no
254   added benefit to yH2AX levels was observed (Fig. S4d). Finally, significant rejuvenation of the
255   DNA methylation clock was observed with 3 of the 4 inhibitors, including Repsox, A83-01, and
256   DMH-1 (Fig. 4d). This data demonstrates that ALK5 and ALK2 inhibition is able reduce DNA
257   damage and restore the DNA methylation clock in this Ercc1 accelerated aging model.
258   RNA-seq analysis was next performed in Ercc1 FBs following treatment with these four TGFb
259   inhibitors to better understand the mechanistic basis for improved DNA damage and a rejuvenated
260   DNA methylation clock with ALK2 or ALK5 inhibition. Notably, PCA scores show the three ALK5
261   inhibitors cluster tightly together compared to the ALK2 inhibitor (Fig. 4e). Interestingly, all 4
262   inhibitors shifted the D/KO transcriptome along the PC2 axis in the direction of WT cells with the
263   greatest change observed following treatment with A83-01 (Fig. 4e). At the same time, Venn
264   diagrams show 558 genes were upregulated and 371 downregulated by all 4 inhibitors indicating
265   similarity in gene expression profile regardless of target receptor (Fig. 4f). Next, gene set

266 enrichment analysis (GSEA) shows significant decreases to spindle checkpoint signaling with
267 Repsox, Vactosertib, and A83-01 but not with DMH-1 (Fig. S4e). DMH-1 had a unique effect on
268 upregulation of response to virus, response to interferon-gamma, and response to interferon-beta
269 among others based on the GSEA (Fig. S4e). Repsox uniquely induced upregulation to
270 developmental-related gene sets including embryonic hindlimb morphogenesis, hindlimb
271 morphogenesis, and midbrain development (Fig. S4e). Reactome analysis showed that DMH-1
272 also uniquely increased interferon signalling (Fig. S4e). Interestingly, GO term analysis
273 demonstrated that all four inhibitors significantly downregulated several biological processes
274 including mitotic cell cycle and canonical glycolysis (Fig. S5a). In line with previous publications
275 showing TGFb inhibition disrupts DNA repair processes in cancer cells and HSCs, these four
276 inhibitors also disrupted several DNA repair proceses in our Ercc1 FBs (Fig. S5a)[65,73–75].
277 Interesting exceptions include a significant improvement to NER by DMH-1 and a trend towards
278 upregulated ICL repair amongst all (Fig. S5a) Together this data shows ALK5 and ALK2 inhibitors
279 are capable of decreasing the DNA damage marker yH2AX and restoring the DNA methylation
280 clock in Ercc1 fibroblasts while sharing some changes to the transcriptomic profiles.

281

282 **TGFb inhibition phenocopies aspects of initiations phase cellular reprogramming**
283 To investigate and compare shared rejuvenation processes between cellular reprogramming and
284 TGFb inhibition, we next evaluated significant transcriptomic changes among the different
285 treatments. Notably, a heatmap of significantly up or down regulated genes among the different
286 treatments indicate a similar profile (Fig. 5c). Specifically, 684 shared DEGs were upregulated and
287 627 downregulated following treatment with the ALK5 inhibitors Repsox, A83-01, Vactosertib, and
288 reprogramming at day 4 (Fig. 5a). Notably, gene expression changes induced by the 4 inhibitors
289 shared a positive correlation with gene expression changes induced by reprogramming (Fig. 5b).
290 The strongest correlation was observed between the three ALK5 inhibitors and D4 reprogramming
291 (Fig. 5b, S5b). Interestingly, A83-01 was the closest in transcriptomic profile to day 4
292 reprogramming while Repsox was the closest to D4 enhanced reprogramming (Fig. 5b, S5b). The
293 top GO terms that were significantly downregulated with either reprogramming or the TGFb
294 inhibitors include external encapsulating structure organization, extracellular matrix organization,
295 extracellular structure organization, collagen fibril organization, skeletal system development and
296 protein hydroxylation (Fig. 5d). The most significantly upregulated GO terms shared by both D4
297 reprogramming and TGFb inhibition include steroid biosynthetic process, regulation. of steroid
298 biosynthetic process, alcohol biosynthetic process, organic hydroxyl compound metabolic process,
299 epidermal cell differentiation, and alcohol metabolic process (Fig. 5d). Reactome analysis of
300 shared processes between reprogramming and Repsox, A83-01, and Vactosertib showed
301 upregulation of complement cascade and downregulation of collagen formation and ECM
302 organization (Fig. 5e).

303

304   Interestingly, significant differences were noted when comparing the transcriptomic effects of
305   reprogramming vs TGFb inhibition on DNA repair processes even though both improved the DNA
306   damage phenotype. Specifically, TGFb inhibition significantly downregulated multiple DNA repair
307   processes in Ercc1 fibroblasts including AltEJ, NHEJ, and HR among others while reprogramming
308   significantly upregulated them (Fig. S5a 3b). At the same time, only DMH-1 matched
309   reprogramming by significantly upregulating NER, while Repsox and Vactosertib showed a trend
310   towards improvment (Fig. s5a). In sum, this transcriptomic data demonstrates that TGFb inhibition
311   and initiation phase reprogramming share a strong correlation in changes to gene expression. At
312   the same time, reprogramming induces a more robust effect, especially on DNA repair processes
313   in our reprogrammable Ercc1 aging model.

314

315   **Discussion**

316   Although the age ameliorating effects of in vivo partial reprogramming have been well documented,
317   the mechanistic drivers of rejuvenation by reprogramming are currently lacking[18]. Interestingly, the
318   robust alterations to biological processes that occurs during the initiation phase of cellular
319   reprogramming including proliferation, chromatin modification, DNA damage repair, MET, and
320   RNA processing are well characterized and could potentially represent mechanistic drivers of
321   longevity[41–45,48]. For these reasons, we investigated the relationship between these early
322   reprogramming induced changes and their impact on aging phenotypes. Specifically, we
323   developed a reprogrammable DNA damage model of accelerated aging, Ercc1$^{\Delta/-}$ 4Fj$^{+/-}$ rtTA$^{+/-}$, in
324   order to test the impact of initiation phase reprogramming on a key driver of aging, genomic
325   instability. As OSKM inhibits TGFb signaling and drives the MET during initiation phase
326   reprogramming, we investigated the mechanistic basis of rejuvenation via cellular reprogramming
327   by comparing it to TGFb inhibition[46]. Due to the slow, stochastic, and asynchronous
328   reprogramming process which confounds molecular studies in bulk cultures we also utilized a
329   previously defined enhanced method of cellular reprogramming by adding ascorbic acid and CHIR-
330   99021 to the culture media[53,56,57].

331

332   Here we observed that OSKM expressing Ercc1 cells undergo robust reprogramming induced
333   changes to morphology, nuclear size, epigenome, transcriptome, and homeostasis related DNA
334   repair processes. Striking improvements to the DNA damage marker yH2AX in our Ercc1
335   fibroblasts with a defective repair process occurred within 2 days of pluripotency factor expression.
336   At the same time, the elevated heterochromatin markers H3K9me3 and H4K20me3 were
337   significantly restored following enhanced reprogramming for 2 and 4 days. Most notably, DNA
338   methylation clock analysis shows significant rejuvenation in these Ercc1 cells after 4 days of
339   enhanced reprogramming. RNA sequencing analysis of the transcriptome showed several GO
340   processes were upregulated significantly including DNA repair, chromatin organization, and mitotic
341   cell cycle. This is consistent with pluripotency transcription factors being upstream of DNA repair

342   processes, particularly DNA double-strand break repair that repairs damage marked by yH2AX[76].

343   Simultaneously, TGFb signaling and EMT processes were significantly downregulated.

344

345   As TGFb signaling is a driver of many aging phenotypes, we further investigated the importance

346   of this signaling pathway to reprogramming induced rejuvenation via inhibition of the TGFb

347   receptor ALK5 or the BMP receptor ALK 2[67,70]. Interestingly, nearly every TGFb inhibitor tested

348   significantly decreased yH2AX levels in Ercc1 fibroblasts. The ALK5 inhibitors showed a more

349   robust impact than ALK2 inhibitors on yH2AX levels while also decreasing nuclear size, a common

350   phenotype observed during reprogramming. Importantly, rejuvenation of the epigenetic clock was

351   observed following treatment with 3 of 4 TGFb inhibitors in this accelerated aging model. At the

352   same time, RNA analysis showed a strong correlation between TGFb inhibition and

353   reprogramming based on similar changes to hundreds of DEGs. Interestingly, the robust changes

354   to DNA repair based on GO pathway analysis was unique to OSKM expression. Previous work

355   has shown that activation of the TFGb pathway promotes genomic instability and induces HR

356   defects while inhibition reduces DNA damage, senescence, and aging phenotypes[67,74,77,78].

357   Interestingly, TGFb inhibition has a disruptive effect on many DNA repair processes while

358   selectively promoting others in a cell type specific manner similar to our observations[65,75].

359

360   Although initiation phase reprogramming in wildtype and Ercc1 fibroblasts was capable of

361   ameliorating the DNA damage marker yH2AX, the scale of effect was far more robust in the DNA

362   damage model as demonstrated by significant increases in all major DNA repair processes. This

363   data suggests that cellular reprogramming is sensitive to intrinsic cell state cues and drives a

364   restoration of homeostatic function and youthful molecular phenotypes. Similarly, in vivo partial

365   reprogramming studies show a more robust improvement to lifespan in progeria models indicating

366   an ability to respond to deleterious cell states[23,25] Previously, it was shown improved DNA repair

367   via overexpression of the HR protein Rad51 enhances reprogramming efficiency[79]. In our 4F Ercc1

368   fibroblasts, we observed the most significant reprogramming-induced rejuvenation coincided with

369   upregulation of multiple DNA repair pathways. Recently maturation phase transient

370   reprogramming for 13 days was shown to reverse the epigenetic clock in aged donors by up to 30

371   years but longer periods saw diminished benefits[33]. Other groups have shown a single short burst

372   of reprogramming in vivo is sufficient to ameliorate aging hallmarks and tissue-specific

373   physiology[25]. The precise mechanism of rejuvenation involved is unknown although several

374   studies, including ours, supports a mechanistic contribution from the epigenetic remodeling

375   process[6,7,32,80]. Importantly, by inducing initiation phase reprogramming in an Ercc1 model with an

376   accelerated epigenetic clock, we observed early reprogramming coincided with TGFb inhibition,

377   improved homeostasis, DNA repair, and epigenetic rejuvenation. Notably, attempts to replicate

378   OSKM-induced TGFb inhibition with small molecule inhibitors phenocopied improvements to the

379   epigenetic clock in this Ercc1 model while decreasing the DNA damage marker yH2AX.

380   Transcriptomic comparisons between cellular reprogramming and TGFb inhibitors of the ALK5 and
381   ALK2 receptors were positively correlated and shared similar changes to hundreds of DEGs. At
382   the same time, the robust upregulation of DNA repair processes via initiation phase reprogramming
383   compared to TGFb inhibition alone suggests a different mechanistic route to DNA damage repair.
384
385   In conclusion, delineating the specific basis of rejuvenation remains difficult and potentially
386   confounded by the multifactorial sequence of events necessary for reprogramming to proceed .
387   The data here supports the premise that TGFb inhibition is a mechanistic contributor to
388   rejuvenation induced by cellular reprogramming. This work sets the stage for further mechanistic
389   investigations into the early events of reprogramming to better understand the associated drivers
390   of rejuvenated phenotypes.
391

392   **Conflict of interest**
393   S.H. is the founder of the non-profit Epigenetic Clock Development Foundation that licenses
394   patents from his former employer UC Regents, and he is listed as the inventor. The remaining
395   authors declare no conflicts of interest.
396

397   **Author contributions**
398   A.O. and P.T.P. designed the study. A.O., A.H., R.B., S.H. and P.T.P. were involved in all
399   experiments, data collection, analysis and interpretation. A.P and P.T.P generated the mice
400   strains. P.T.P. and C.R. prepared the figures. C.M. performed skin fibroblast extractions. C.R.,
401   F.M., A.S., V.G. and P.T.P. prepared and analyzed RNA-seq data. A.O., P.T.P., and G.M. provided
402   guidance. P.T.P wrote the manuscript with input from authors.
403

404   **Data availability statement**
405   The data can be made available from the corresponding author upon request.
406   The mammalian methylation array is from the nonprofit Epigenetic Clock Development Foundation
407   (https://clockfoundation.org/).
408

409   **Code availability statement**
410   The RNA-seq analysis code is available at https://github.com/cheyennerechsteiner/Ercc1-
411   Reprogramming.
412

413   **Methods**
414   **Animal housing**
415   These experiments were performed in accordance with Swiss legislation and after approval from
416   the local authorities (Cantonal veterinary office, Canton de Vaud, Switzerland). Mice were housed
417   in groups of five per cage or less with a 12hr light/dark cycle between 06:00 and 18:00 in a

11

418 temperature-controlled environment at 25°C and humidity between 40 % and 70 %, with access to
419 water and food. Wild type, premature aging, and programmable mouse models generated were
420 housed together in the Animal Facilities of Epalinges and Department of Biomedical Science of
421 the University of Lausanne.
422

Mouse strains

424 Ercc1$^{\Delta/-}$ mice and littermate controls Ercc1$^{+/+}$ were generated in a C57BL6J|FVB hybrid
425 background as previously generated and described by de Waard [13]. Reprogrammable 4Fj$^{+/-}$ rtTA$^{+/-}$
426 Ercc1$^{\Delta/-}$ (4F.D/KO) and 4Fj$^{+/-}$ rtTA$^{+/-}$ Ercc1$^{+/+}$ (4F.WT) mice strains were generated in a
427 C57BL6J|FVB hybrid background following crosses with the previously described 4Fj mouse
428 developed by Rudolf Jaenisch [82]. Previously described wildtype reprogrammable cells with an
429 Oct4-EGFP reporter were derived from mice carrying a polycistronic cassette containing Oct4,
430 Sox2, Klf4, c-Myc, and a single allele EGFP in the Col1a1 locus (OKSM)[83].
431

Mouse monitoring and euthanasia

433 All mice were monitored three times per week for their activity, posture, alertness, body weight,
434 presence of tumors or wound, and surface temperature. Males and females were euthanized at by
435 CO_2 inhalation (6 min, flow rate 20% volume/min). Subsequently, tail tip fibroblasts were harvested
436 and cultured.
437

Cell culture and maintenance

439 Tail tip fibroblasts (TTF) were extracted from mice using Collagenase I (Sigma, C0130) and
440 Dispase II (Sigma, D4693) and cultured in DMEM (Gibco, 11960085) containing 1% non-essential
441 amino acids (Gibco, 11140035), 1% GlutaMax (Gibco, 35050061), 1% Sodium Pyruvate (Gibco,
442 11360039) and 10% fetal bovine serum (FBS, Hyclone, SH30088.03) at 37°C in hypoxic conditions
443 (3% O2). Subsequently, fibroblasts were cultured and passaged (3 or less) according to standard
444 protocols. Reprogrammable TTF cells used in experiments were from young mice, including 4Fj$^{+/-}$
445 rtTA$^{+/-}$ Ercc1$^{\Delta/-}$ and 4Fj$^{+/-}$ rtTA$^{+/-}$ Ercc1$^{+/+}$ (8 week old male), and 4FJ$^{+/-}$ OCT4-GFP TTF (22 week
446 old female). Non-reprogramming Ercc1 TTF used include Ercc1$^{\Delta/-}$ and Ercc1$^{+/+}$ (8 week old male)
447 Experiments for TGFb inhibitors used Ercc1$^{\Delta/-}$ cells (4 week old female) and Ercc1$^{+/+}$ TTF cells (14
448 week old female). Induction of the OSKM reprogramming factors in vitro followed treatment with
449 doxycycline 2ug/ml in culture media for the specified time points. Enhanced reprogramming
450 followed the same protocols but added fresh ascorbic acid (50ug/ml) and CHIR-99201 (3uM) as
451 previously reported[53].
452

Immunofluorescence staining

454 Following experiments in 96 well plates or 24 well plates, TTF were washed with fresh PBS and
455 fixed with 4% paraformaldehyde (Roth, 0964.1) in PBS at room temperature (RT) for 15 minutes.

456 Then cells were washed 3 more times, followed by blocking and permeabilization step in 1% bovine

457 serum albumin (Sigma, A9647-50G) in PBST (0.2% Triton X-100 in PBS) for 1 hour (Roth, 3051.3).

458 TTF were then incubated at 4°C overnight with a primary antibody, washed in PBS, followed by

459 incubation with a secondary antibody and DAPI staining at room temp. for 1 hour. If performed in

460 24 well plates, coverslips were used and mounted with Fluoromount-G (Thermofisher, 00-4958-

461 02), dried at RT in the dark, and stored at 4°C until ready to image or -20°C for long-term.

462

463 **Immunofluorescence imaging**

464 Confocal image acquisition was performed using the NIKON Ti2 Yokogawa CSU-W1 Spinning

465 Disk, using the 100X objective and with 15 z-sections of 0.3 μm intervals. Lasers for each antibody

466 were selected (405 nm and 488 nm) with a typical laser intensity set. Exposure time and binning

467 were established separately to assure avoidance of signal saturation.

468

469 **Antibodies and compounds**

470 Antibodies include: Abcam: anti-H3K27me3 (ab192985); Cell Signaling: anti-H3K9me3 (13969),

471 anti-H4K20me3, anti-γH2AX (9718); Roth: DAPI (6843.1) Compounds include: Cayman; Valproic

472 Acid (13033), CHIR99021 (13122), Repsox (14794), Forskolin (11018), Doxorubicin (15007);

473 Acros Organics: TCP (130472500); APExBIO: DZNep (A8182); Seleckchem: TTNPB (S4627);

474 Roth: X-beta-Gal (2315.3), Ascorbic Acid (Sigma).

475

476 **Flow cytometry**

477 Cells were stained with Thy1.2-APC and SSEA1-PE (Biolegend). Cells were fixed in BD Fixation

478 and Permeabilization Solution. A Bechman Coulter Cytoflex S flow cytometer determined cellular

479 subpopulation ratios.

480

481 **RNA sequencing, processing, analysis**

482 Total RNA and DNA was extracted from the same samples. Total RNA was extracted from cells

483 using the Qiagen AllPrep DNA/RNA Micro Kit (New England Biolab) and protocols were followed.

484 Total RNA concentrations were determined using the Qubit RNA BR Assay Kit (Thermofisher,

485 Q10211).

486

487 The RNA-Seq library preparation and sequencing was done by Novogene (UK) Company Limited

488 on an Illumina NovaSeq 6000 in 150 bp paired-end mode. Raw FASTQ files were evaluated for

489 quality, adapter content and duplication rates with FastQC. Reads were trimmed using TrimGalore!

490 (https://www.bioinformatics.babraham.ac.uk/projects/trim_galore/) and aligned to the GRCm39

491 mouse genome assembly using Hisat2 (https://doi.org/10.1038/s41587-019-0201-4). Number of

492 reads per gene were measured using the featureCounts function in the subread package[84].

493

494   All subsequent analysis was performed in R. DESeq2 was used to normalize raw read counts and

495   perform differential gene expression analysis (doi:10.1186/s13059-014-0550-8). Ensembl gene

496   IDs were mapped to gene symbols via the mapIds function in the AnnotationDbi package (Pagès

497   H, Carlson M, Falcon S, Li N (2023). *AnnotationDbi: Manipulation of SQLite-based annotations in*

498   *Bioconductor*) with an org.Mm.eg.db reference package (Carlson M (2019). *org.Mm.eg.db:*

499   *Genome wide annotation for Mouse*). The clusterProfiler package (doi:10.1089/omi.2011.0118,

500   doi:10.1016/j.xinn.2021.100141) was used to perform gene set enrichment analysis (GSEA) on

501   gene ontology and Reactome terms.

502

503   **DNA extractions**

504   Total DNA was extracted from cells using the Qiagen AllPrep DNA/RNA Micro Kit (New England

505   Biolab) and protocols were followed. Total DNA concentrations were determined with the Qubit

506   DNA BR Assay (Thermofisher, Q10211).

507

508   **DNA methylation clock**

509   Methylation data was generated via the HorvathMammalMethylChip[85] and normalized with the

510   SeSaMe method[86]. Human methylation data were generated on the Illumina EPIC array platforms

511   which profiles 866k cytosines. The noob normalization method was used and implemented in the

512   R function preprocess Noob. The DNAm age was estimated using the DNAm Age Skin Final clock

513   algorithm.[87]

514

515   **MTS cell proliferation assay**

516   Cell viability was performed with Tetrazolium MTS assay. Cells were cultured for 1 day in 96-well

517   plates and treated with small molecules for 3 consecutive days prior to incubation with 120 µL fresh

518   media containing 20 µL of CellTiter 96® AQueous One Solution (Promega, G3580) for 1 to 4 hours

519   at 37°C in a humidified, 5% CO_2 atmosphere. The absorbance was determined at 490nm using a

520   BioTek Epoch 2 microplate reader. The proportion of viable cells was determined as a ratio

521   between the observed optical density (OD) compared to control OD.

522

523   **Quantification and statistical analysis**

524   Analysis of immunofluorescence microscopy images was performed using FIJI. Typically, 20

525   different ROIs were imaged at 100x from each well from three experiments unless otherwise noted.

526   Maximal projections of z-stacks were analyzed and total fluorescence intensity per cell and total

527   nuclear area were determined.

528

529   All statistical analysis, statistical significance and n values are reported in the figure legends.

530   Statistical analyses were performed using GraphPad Prism 9.0.0.

531

References

1. Rando, T. A. & Chang, H. Y. Aging, Rejuvenation, and Epigenetic Reprogramming: Resetting the Aging Clock. *Cell* **148**, 46–57 (2012).

2. Kennedy, B. K. *et al.* Geroscience: Linking Aging to Chronic Disease. *Cell* **159**, 709–713 (2014).

3. López-Otín, C., Blasco, M. A., Partridge, L., Serrano, M. & Kroemer, G. The Hallmarks of Aging. *Cell* **153**, 1194–1217 (2013).

4. Schumacher, B., Pothof, J., Vijg, J. & Hoeijmakers, J. H. J. The central role of DNA damage in the ageing process. *Nature* **592**, 695–703 (2021).

5. Niedernhofer, L. J. *et al.* Nuclear Genomic Instability and Aging. *Annu. Rev. Biochem.* **87**, 295–322 (2018).

6. Yang, J.-H. *et al.* Loss of epigenetic information as a cause of mammalian aging. *Cell* **186**, 305-326.e27 (2023).

7. Kane, A. E. & Sinclair, D. A. Epigenetic changes during aging and their reprogramming potential. *Crit. Rev. Biochem. Mol. Biol.* **54**, 61–83 (2019).

8. Tubbs, A. & Nussenzweig, A. Endogenous DNA Damage as a Source of Genomic Instability in Cancer. *Cell* **168**, 644–656 (2017).

9. Vermeij, W. P. *et al.* Restricted diet delays accelerated ageing and genomic stress in DNA-repair-deficient mice. *Nature* **537**, 427–431 (2016).

10. Li, W. *et al.* Nucleotide excision repair capacity increases during differentiation of human embryonic carcinoma cells into neurons and muscle cells. *J. Biol. Chem.* **294**, 5914–5922 (2019).

11. Weeda, G. *et al.* Disruption of mouse ERCC1 results in a novel repair syndrome with growth failure, nuclear abnormalities and senescence. *Curr. Biol.* **7**, 427–439 (1997).

12. Dollé, M. E. T. *et al.* Increased genomic instability is not a prerequisite for shortened lifespan in DNA repair deficient mice. *Mutat. Res. Mol. Mech. Mutagen.* **596**, 22–35 (2006).

13. de Waard, M. C. *et al.* Age-related motor neuron degeneration in DNA repair-deficient Ercc1 mice. *Acta Neuropathol. (Berl.)* **120**, 461–475 (2010).

561   14. Tian, X. *et al.* SIRT6 Is Responsible for More Efficient DNA Double-Strand Break Repair in

562   Long-Lived Species. *Cell* **177**, 622-638.e22 (2019).

563   15. Takayama, K. *et al.* mTOR signaling plays a critical role in the defects observed in muscle-

564   derived stem/progenitor cells isolated from a murine model of accelerated aging. *J. Orthop.*

565   *Res.* **35**, 1375–1382 (2017).

566   16. Birkisdóttir, M. B. *et al.* Unlike dietary restriction, rapamycin fails to extend lifespan and

567   reduce transcription stress in progeroid DNA repair-deficient mice. *Aging Cell* **20**, e13302

568   (2021).

569   17. Takahashi, K. & Yamanaka, S. Induction of Pluripotent Stem Cells from Mouse Embryonic

570   and Adult Fibroblast Cultures by Defined Factors. *Cell* **126**, 663–676 (2006).

571   18. Singh, P. B. & Newman, A. G. Age reprogramming and epigenetic rejuvenation. *Epigenetics*

572   *Chromatin* **11**, 73 (2018).

573   19. Lapasset, L. *et al.* Rejuvenating senescent and centenarian human cells by reprogramming

574   through the pluripotent state. *Genes Dev.* **25**, 2248–2253 (2011).

575   20. Mahmoudi, S., Xu, L. & Brunet, A. Turning back time with emerging rejuvenation strategies.

576   *Nat. Cell Biol.* **21**, 32–43 (2019).

577   21. de Magalhães, J. P. & Ocampo, A. Cellular reprogramming and the rise of rejuvenation

578   biotech. *Trends Biotechnol.* **40**, 639–642 (2022).

579   22. Alle, Q., Le Borgne, E., Milhavet, O. & Lemaitre, J.-M. Reprogramming: Emerging Strategies

580   to Rejuvenate Aging Cells and Tissues. *Int. J. Mol. Sci.* **22**, 3990 (2021).

581   23. Ocampo, A. *et al.* In Vivo Amelioration of Age-Associated Hallmarks by Partial

582   Reprogramming. *Cell* **167**, 1719-1733.e12 (2016).

583   24. Macip, C. C. *et al.* Gene Therapy Mediated Partial Reprogramming Extends Lifespan and

584   Reverses Age-Related Changes in Aged Mice. 2023.01.04.522507 Preprint at

585   https://doi.org/10.1101/2023.01.04.522507 (2023).

586   25. Alle, Q. *et al.* A single short reprogramming early in life initiates and propagates an

587   epigenetically related mechanism improving fitness and promoting an increased healthy

588   lifespan. *Aging Cell* **21**, e13714 (2022).

589   26. Sarkar, T. J. *et al.* Transient non-integrative expression of nuclear reprogramming factors

590   promotes multifaceted amelioration of aging in human cells. *Nat. Commun.* **11**, 1545 (2020).

591   27. de Lázaro, I. *et al.* Non-viral, Tumor-free Induction of Transient Cell Reprogramming in

592   Mouse Skeletal Muscle to Enhance Tissue Regeneration. *Mol. Ther.* **27**, 59–75 (2019).

593   28. Wang, C. *et al.* In vivo partial reprogramming of myofibers promotes muscle regeneration by

594   remodeling the stem cell niche. *Nat. Commun.* **12**, 3094 (2021).

595   29. Browder, K. C. *et al.* In vivo partial reprogramming alters age-associated molecular changes

596   during physiological aging in mice. *Nat. Aging* **2**, 243–253 (2022).

597   30. Chen, Y. *et al.* Reversible reprogramming of cardiomyocytes to a fetal state drives heart

598   regeneration in mice. *Science* **373**, 1537–1540 (2021).

599   31. Cheng, F. *et al.* Partial reprogramming strategy for intervertebral disc rejuvenation by

600   activating energy switch. *Aging Cell* **21**, e13577 (2022).

601   32. Lu, Y. *et al.* Reprogramming to recover youthful epigenetic information and restore vision.

602   *Nature* **588**, 124–129 (2020).

603   33. Gill, D. *et al.* Multi-omic rejuvenation of human cells by maturation phase transient

604   reprogramming. *eLife* **11**, e71624 (2022).

605   34. Chondronasiou, D. *et al.* Multi-omic rejuvenation of naturally aged tissues by a single cycle of

606   transient reprogramming. *Aging Cell* **21**, e13578 (2022).

607   35. Maherali, N. *et al.* Directly Reprogrammed Fibroblasts Show Global Epigenetic Remodeling

608   and Widespread Tissue Contribution. *Cell Stem Cell* **1**, 55–70 (2007).

609   36. Mikkelsen, T. S. *et al.* Dissecting direct reprogramming through integrative genomic analysis.

610   *Nature* **454**, 49–55 (2008).

611   37. Brambrink, T. *et al.* Sequential Expression of Pluripotency Markers during Direct

612   Reprogramming of Mouse Somatic Cells. *Cell Stem Cell* **2**, 151–159 (2008).

613   38. Plath, K. & Lowry, W. E. Progress in understanding reprogramming to the induced

614   pluripotent state. *Nat. Rev. Genet.* **12**, 253–265 (2011).

615   39. Stadtfeld, M., Maherali, N., Breault, D. T. & Hochedlinger, K. Defining Molecular

616   Cornerstones during Fibroblast to iPS Cell Reprogramming in Mouse. *Cell Stem Cell* **2**, 230–

617   240 (2008).

17

618   40. Li, R. *et al.* A Mesenchymal-to-Epithelial Transition Initiates and Is Required for the Nuclear

619   Reprogramming of Mouse Fibroblasts. *Cell Stem Cell* **7**, 51–63 (2010).

620   41. Samavarchi-Tehrani, P. *et al.* Functional Genomics Reveals a BMP-Driven Mesenchymal-to-

621   Epithelial Transition in the Initiation of Somatic Cell Reprogramming. *Cell Stem Cell* **7**, 64–77

622   (2010).

623   42. Polo, J. M. *et al.* A Molecular Roadmap of Reprogramming Somatic Cells into iPS Cells. *Cell*

624   **151**, 1617–1632 (2012).

625   43. Buganim, Y. *et al.* Single-Cell Expression Analyses during Cellular Reprogramming Reveal

626   an Early Stochastic and a Late Hierarchic Phase. *Cell* **150**, 1209–1222 (2012).

627   44. Benevento, M. *et al.* Proteome adaptation in cell reprogramming proceeds via distinct

628   transcriptional networks. *Nat. Commun.* **5**, 5613 (2014).

629   45. Hansson, J. *et al.* Highly Coordinated Proteome Dynamics during Reprogramming of

630   Somatic Cells to Pluripotency. *Cell Rep.* **2**, 1579–1592 (2012).

631   46. David, L. & Polo, J. M. Phases of reprogramming. *Stem Cell Res.* **12**, 754–761 (2014).

632   47. Kuno, A., Nishimura, K. & Takahashi, S. Time-course transcriptome analysis of human

633   cellular reprogramming from multiple cell types reveals the drastic change occurs between

634   the mid phase and the late phase. *BMC Genomics* **19**, 9 (2018).

635   48. Koche, R. P. *et al.* Reprogramming Factor Expression Initiates Widespread Targeted

636   Chromatin Remodeling. *Cell Stem Cell* **8**, 96–105 (2011).

637   49. Roux, A. E. *et al.* Diverse partial reprogramming strategies restore youthful gene expression

638   and transiently suppress cell identity. *Cell Syst.* **13**, 574-587.e11 (2022).

639   50. Mahmoudi, S. *et al.* Heterogeneity in old fibroblasts is linked to variability in reprogramming

640   and wound healing. *Nature* **574**, 553–558 (2019).

641   51. Ebrahimi, B. Reprogramming barriers and enhancers: strategies to enhance the efficiency

642   and kinetics of induced pluripotency. *Cell Regen.* **4**, 10 (2015).

643   52. Stadtfeld, M. & Hochedlinger, K. Induced pluripotency: history, mechanisms, and

644   applications. *Genes Dev.* **24**, 2239–2263 (2010).

645   53. Bar-Nur, O. *et al.* Small molecules facilitate rapid and synchronous iPSC generation. *Nat.*

646   *Methods* **11**, 1170–1176 (2014).

647 54. Vidal, S. E., Amlani, B., Chen, T., Tsirigos, A. & Stadtfeld, M. Combinatorial Modulation of

648   Signaling Pathways Reveals Cell-Type-Specific Requirements for Highly Efficient and

649   Synchronous iPSC Reprogramming. *Stem Cell Rep.* **3**, 574–584 (2014).

650 55. Chen, J. *et al.* Rational optimization of reprogramming culture conditions for the generation

651   of induced pluripotent stem cells with ultra-high efficiency and fast kinetics. *Cell Res.* **21**,

652   884–894 (2011).

653 56. Li, W. *et al.* Generation of Human-Induced Pluripotent Stem Cells in the Absence of

654   Exogenous Sox2. *Stem Cells* **27**, 2992–3000 (2009).

655 57. Liu, X. *et al.* Ascorbic Acid in Epigenetic Reprogramming. *Curr. Stem Cell Res. Ther.* **17**, 13–

656   25 (2022).

657 58. Esteban, M. A. *et al.* Vitamin C Enhances the Generation of Mouse and Human Induced

658   Pluripotent Stem Cells. *Cell Stem Cell* **6**, 71–79 (2010).

659 59. Perez, K. *et al.* ERCC1 mice, unlike other premature aging models, display accelerated

660   epigenetic age. 2022.12.28.522011 Preprint at https://doi.org/10.1101/2022.12.28.522011

661   (2022).

662 60. Horvath, S. DNA methylation age of human tissues and cell types. *Genome Biol.* **14**, 3156

663   (2013).

664 61. Olova, N., Simpson, D. J., Marioni, R. E. & Chandra, T. Partial reprogramming induces a

665   steady decline in epigenetic age before loss of somatic identity. *Aging Cell* **18**, e12877

666   (2019).

667 62. Takata, H. *et al.* Chromatin Compaction Protects Genomic DNA from Radiation Damage.

668   *PLoS ONE* **8**, e75622 (2013).

669 63. Lee, J.-H., Kim, E. W., Croteau, D. L. & Bohr, V. A. Heterochromatin: an epigenetic point of

670   view in aging. *Exp. Mol. Med.* **52**, 1466–1474 (2020).

671 64. Mah, N. *et al.* Molecular Insights into Reprogramming-Initiation Events Mediated by the

672   OSKM Gene Regulatory Network. *PLOS ONE* **6**, e24351 (2011).

673 65. Liu, Q. *et al.* Loss of TGFβ signaling increases alternative end-joining DNA repair that

674   sensitizes to genotoxic therapies across cancer types. *Sci. Transl. Med.* **13**, eabc4465

675   (2021).

19

66. Kim, B.-G., Malek, E., Choi, S. H., Ignatz-Hoover, J. J. & Driscoll, J. J. Novel therapies emerging in oncology to target the TGF-β pathway. *J. Hematol. Oncol.J Hematol Oncol* **14**, 55 (2021).

67. Tominaga, K. & Suzuki, H. I. TGF-β Signaling in Cellular Senescence and Aging-Related Pathology. *Int. J. Mol. Sci.* **20**, 5002 (2019).

68. Lyu, G. *et al.* TGF-β signaling alters H4K20me3 status via miR-29 and contributes to cellular senescence and cardiac aging. *Nat. Commun.* **9**, 2560 (2018).

69. Schoenfeldt, L. *et al.* Chemical reprogramming ameliorates cellular hallmarks of aging and extends lifespan. 2022.08.29.505222 Preprint at https://doi.org/10.1101/2022.08.29.505222 (2022).

70. Weiss, A. & Attisano, L. The TGFbeta Superfamily Signaling Pathway. *WIREs Dev. Biol.* **2**, 47–63 (2013).

71. Hou, P. *et al.* Pluripotent Stem Cells Induced from Mouse Somatic Cells by Small-Molecule Compounds. *Science* **341**, 651–654 (2013).

72. Guan, J. *et al.* Chemical reprogramming of human somatic cells to pluripotent stem cells. *Nature* **605**, 325–331 (2022).

73. Liu, Q., Lopez, K., Murnane, J., Humphrey, T. & Barcellos-Hoff, M. H. Misrepair in Context: TGFβ Regulation of DNA Repair. *Front. Oncol.* **9**, (2019).

74. Pal, D. *et al.* TGF-β reduces DNA ds-break repair mechanisms to heighten genetic diversity and adaptability of CD44+/CD24− cancer cells. *eLife* **6**, e21615 (2017).

75. Zhang, H. *et al.* TGF-β Inhibition Rescues Hematopoietic Stem Cell Defects and Bone Marrow Failure in Fanconi Anemia. *Cell Stem Cell* **18**, 668–681 (2016).

76. Lu, J. Y. *et al.* Comparative transcriptomics reveals circadian and pluripotency networks as two pillars of longevity regulation. *Cell Metab.* **34**, 836-856.e5 (2022).

77. Kanamoto, T., Hellman, U., Heldin, C.-H. & Souchelnytskyi, S. Functional proteomics of transforming growth factor-β1-stimulated Mv1Lu epithelial cells: Rad51 as a target of TGFβ1-dependent regulation of DNA repair. *EMBO J.* **21**, 1219–1230 (2002).

78. Liu, L. *et al.* TGFβ Induces "BRCAness" and Sensitivity to PARP Inhibition in Breast Cancer by Regulating DNA-Repair Genes. *Mol. Cancer Res.* **12**, 1597–1609 (2014).

705   79. Lee, J.-Y., Kim, D.-K., Ko, J.-J., Kim, K. P. & Park, K.-S. Rad51 Regulates Reprogramming

706   Efficiency through DNA Repair Pathway. *Dev. Reprod.* **20**, 163–169 (2016).

707   80. Manukyan, M. & Singh, P. B. Epigenome rejuvenation: HP1β mobility as a measure of

708   pluripotent and senescent chromatin ground states. *Sci. Rep.* **4**, 4789 (2014).

709   81. López-León, M., Outeiro, T. F. & Goya, R. G. Cell reprogramming: Therapeutic potential and

710   the promise of rejuvenation for the aging brain. *Ageing Res. Rev.* **40**, 168–181 (2017).

711   82. Carey, B. W., Markoulaki, S., Beard, C., Hanna, J. & Jaenisch, R. Single-gene transgenic

712   mouse strains for reprogramming adult somatic cells. *Nat. Methods* **7**, 56–59 (2010).

713   83. Stadtfeld, M., Maherali, N., Borkent, M. & Hochedlinger, K. A reprogrammable mouse strain

714   from gene-targeted embryonic stem cells. *Nat. Methods* **7**, 53–55 (2010).

715   84. Liao, Y., Smyth, G. K. & Shi, W. The Subread aligner: fast, accurate and scalable read

716   mapping by seed-and-vote. *Nucleic Acids Res.* **41**, e108 (2013).

717   85. Arneson, A. *et al.* A mammalian methylation array for profiling methylation levels at

718   conserved sequences. *Nat. Commun.* **13**, 783 (2022).

719   86. Zhou, W., Triche, T. J., Jr, Laird, P. W. & Shen, H. SeSAMe: reducing artifactual detection of

720   DNA methylation by Infinium BeadChips in genomic deletions. *Nucleic Acids Res.* **46**, e123

721   (2018).

722   87. Boroni, M. *et al.* Highly accurate skin-specific methylome analysis algorithm as a platform to

723   screen and validate therapeutics for healthy aging. *Clin. Epigenetics* **12**, 105 (2020).
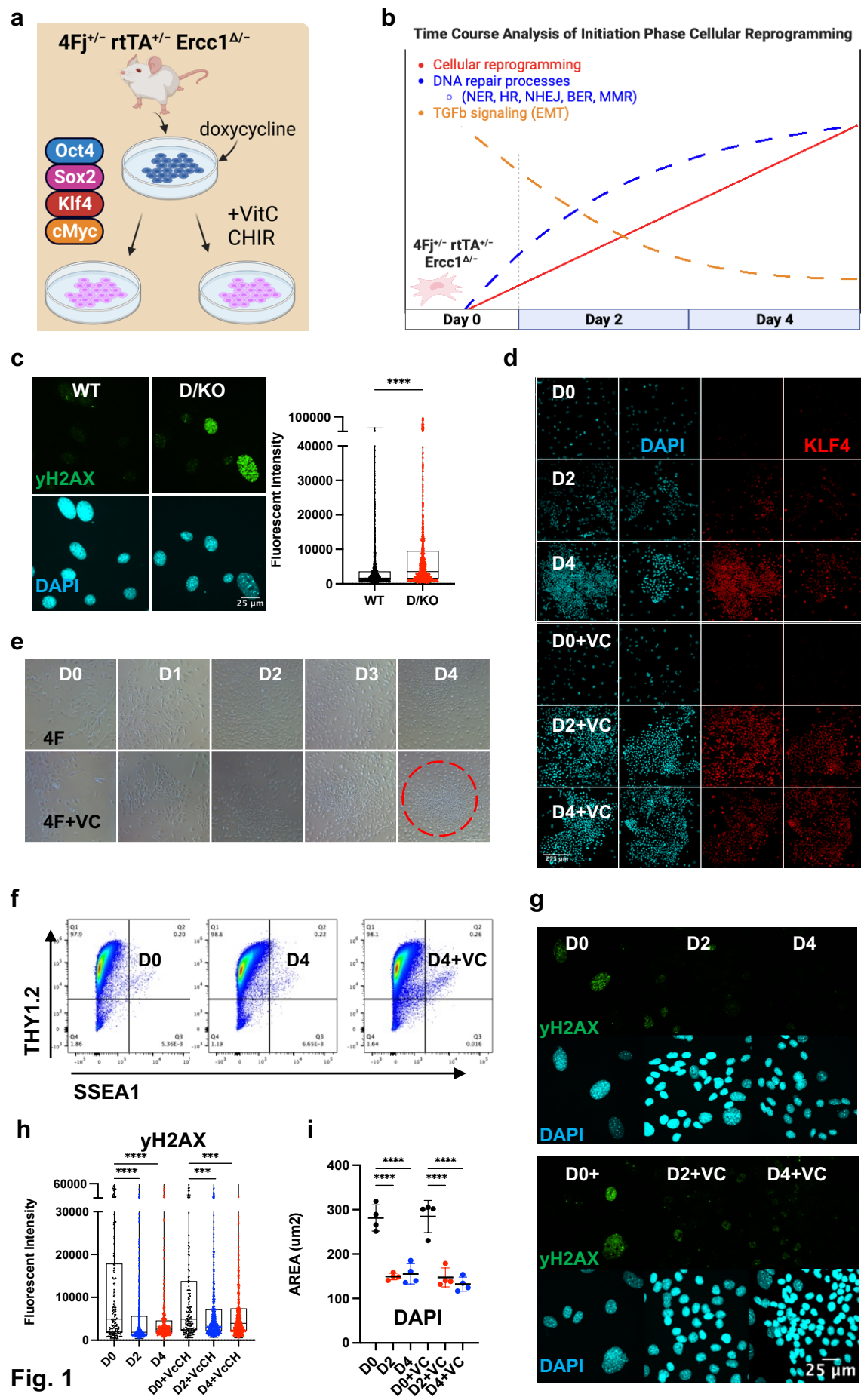
724

Fig. 1

Figure 1: Initiation phase reprogramming in 4Fj$^{+/-}$ rtTA$^{+/-}$ Ercc1$^{\Delta/-}$ accelerated aging model promotes DNA damage repair.

(a) Illustration of doxycycline inducible cellular reprogramming Ercc1 mutant fibroblasts (Fb) alone or enhanced with small molecules. **(b)** Schematic of initiation phase timecourse analysis setup with observed changes to DNA repair and TGFb signaling. **(c)** Representative Immunofluorescence (IF) and quantification of yH2AX in fibroblasts from wildtype (WT) and Ercc1$^{\Delta/-}$ (D/KO) mice, imaged with Nikon laser confocal spinning disc, according to Mann-Whitney test, **** $p<0.0001$. **(d)** IF of KLF4 and DAPI in 4Fj$^{+/-}$ rtTA$^{+/-}$ Ercc1$^{\Delta/-}$ Fbs after 2 and 4 days doxycycline induction with or without VC at 100x **(e)** Time course analysis of 4F and 4F.D/KO Fb during 4 days of dox induction +/- VC, brightfield (BF) images at 4x. **(f)** FACS analysis of reprogramming FBs at day 0 and day 4, stained with Thy1.2 and SSEA1. **(g)** IF of yH2AX and DAPI during time course analysis of 4F.D/KO Fb +/-VC. **(h)** IF quantification of yH2AX levels during timecourse shows decrease levels at day 2 and day 4 according to one way ANOVA, *** $p<0.001$. **(i)** Quantification of DAPI area during timecourse shows decrease in size at day 2 and day 4 based on mean values of 4 experiments according to one way ANOVA, **** $p<0.0001$.
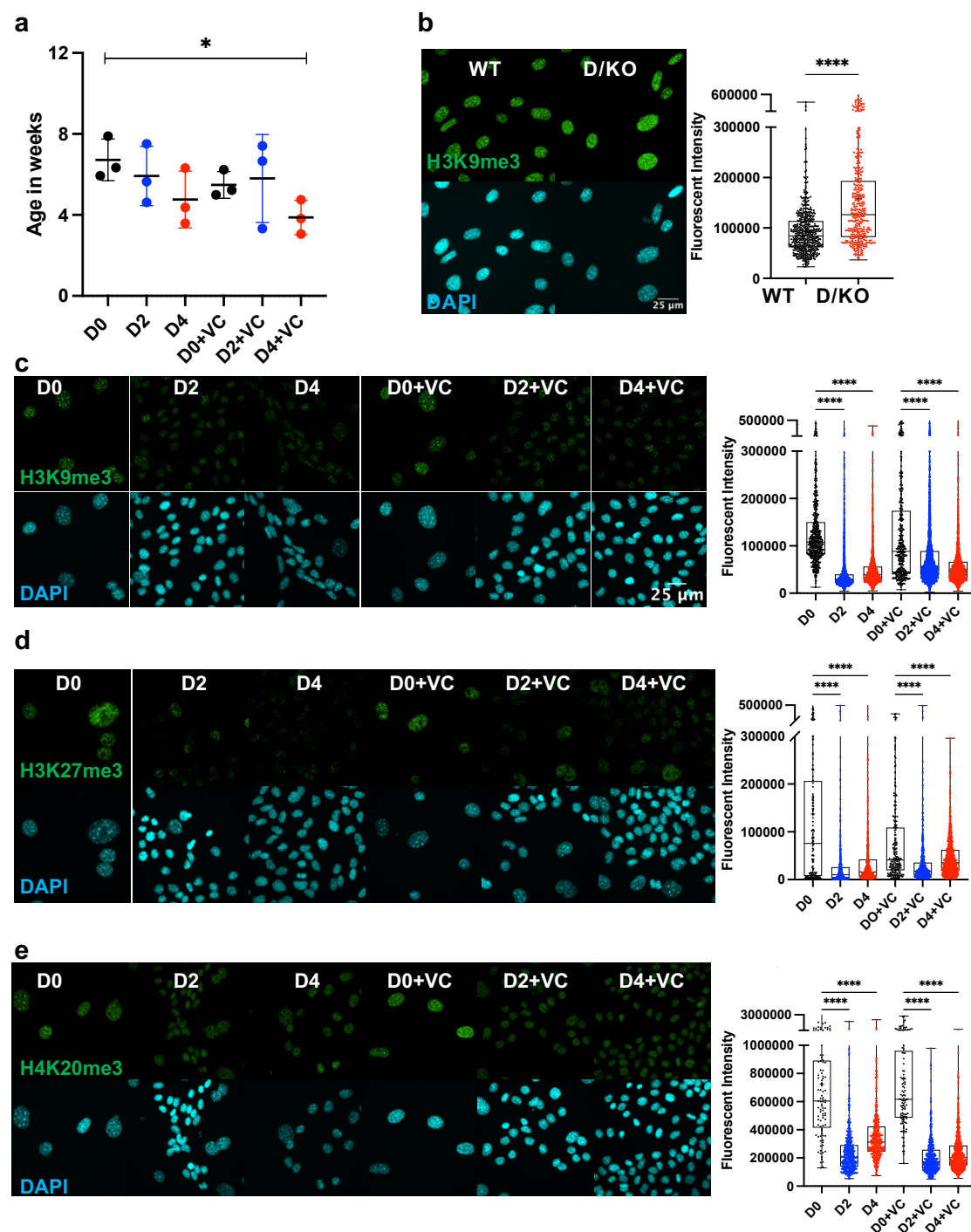
Fig. 2

Figure 2: DNA methylation clock is restored in Ercc1$^{\Delta/-}$ following short term reprogramming.

(a) DNA methylation clock (DNA Methylation Age Skin Final clock) analysis of cellular Ercc1 mutant Fb during time course, n = 3, * p<0.05 according to unpaired t-test. **(b)** IF and quantification of H3K9me3 in fibroblasts from WT and D/KO mice, imaged with Nikon laser confocal spinning disc, according to Mann-Whitney test, **** p<0.0001. **(c)** IF and quantification of H3K9me3 and DAPI during time course in 4F.D/KO Fbs after 2 and 4 days doxycycline induction with or without VC at 100x according to Kruskal-Wallis test, * p<0.0001 **(d)** IF and quantification of H3K27me3 and DAPI during time course in 4F.D/KO Fbs after 2 and 4 days doxycycline induction with or without VC at 100x according to Kruskal-Wallis test, * p<0.0001 **(e)** IF and quantification of H4K20me3 and DAPI during time course in 4F.D/KO Fbs after 2 and 4 days doxycycline induction with or without VC at 100x according to Kruskal-Wallis test, * p<0.0001.
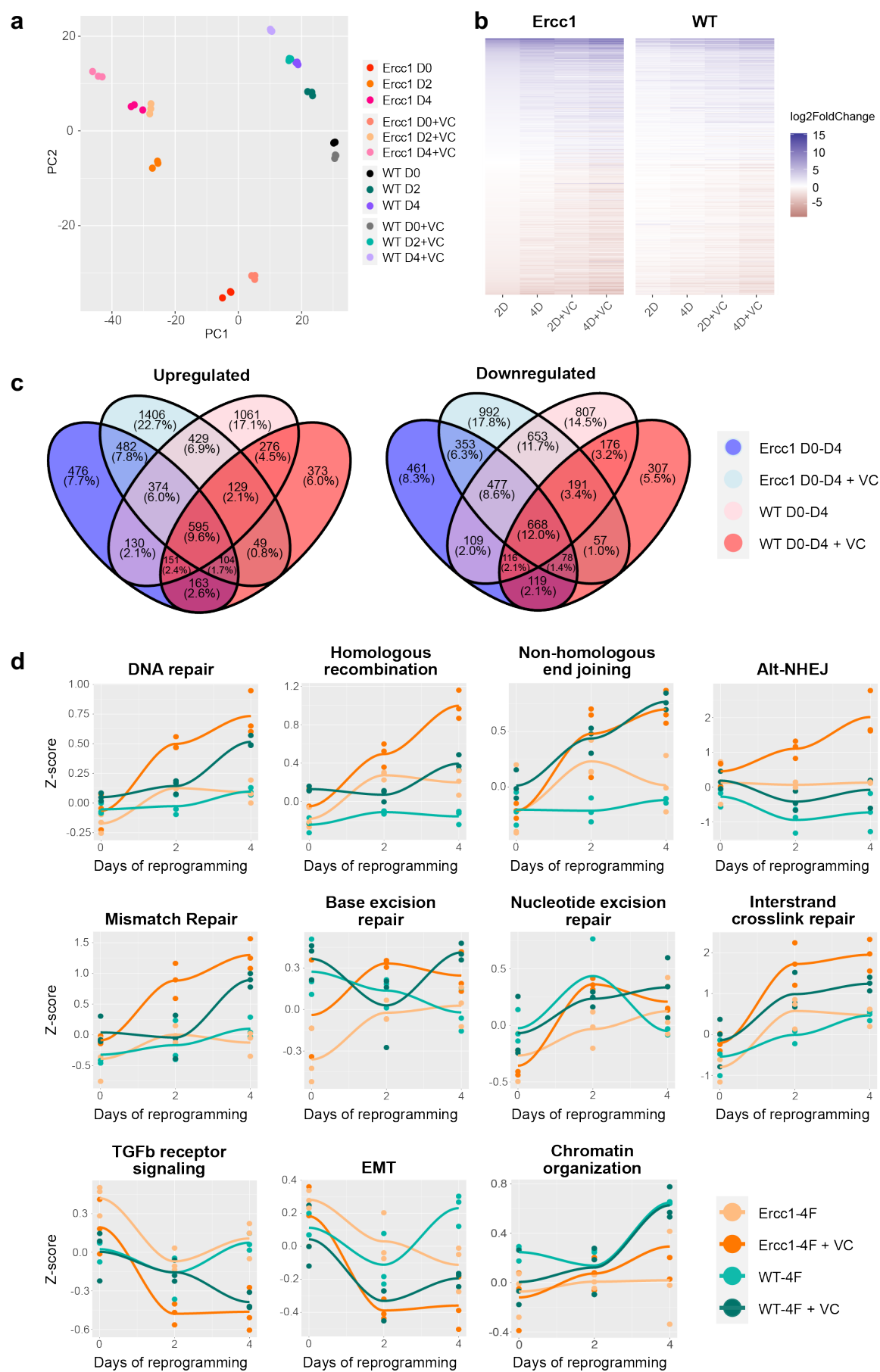
Fig. 3

Figure 3: Initation phase reprogramming drives transcriptomic reset and upregulates DNA repair and chromatin organization in Ercc1$^{\Delta/-}$

(a) Principal component analysis (PCA) of the Ercc1 and WT reprogramming at days 0, 2, and 4 with and without VC enhancement. Principal components 1 and 2 are shown. **(b)** Heat map comparing Ercc1 and WT reprogramming at all timepoints, models, and treatements. Genes with a p-value lower than 1e-18 in at least one condition are shown. **(c)** Venn Diagram showing the overlap of significant DEGs (adjusted p-value < 0.05) in Ercc1 and WT during IP reprogramming with and without VC enhancement. Genes were evaluated using a continuous model over 4 days of reprogramming. **(d)** Reprogramming trajectory visualizations based on median Z-scores of genes from significantly up or down regulated GO pathway including DNA repair, TGFb signaling, EMT, and chromatin organization (n=3).
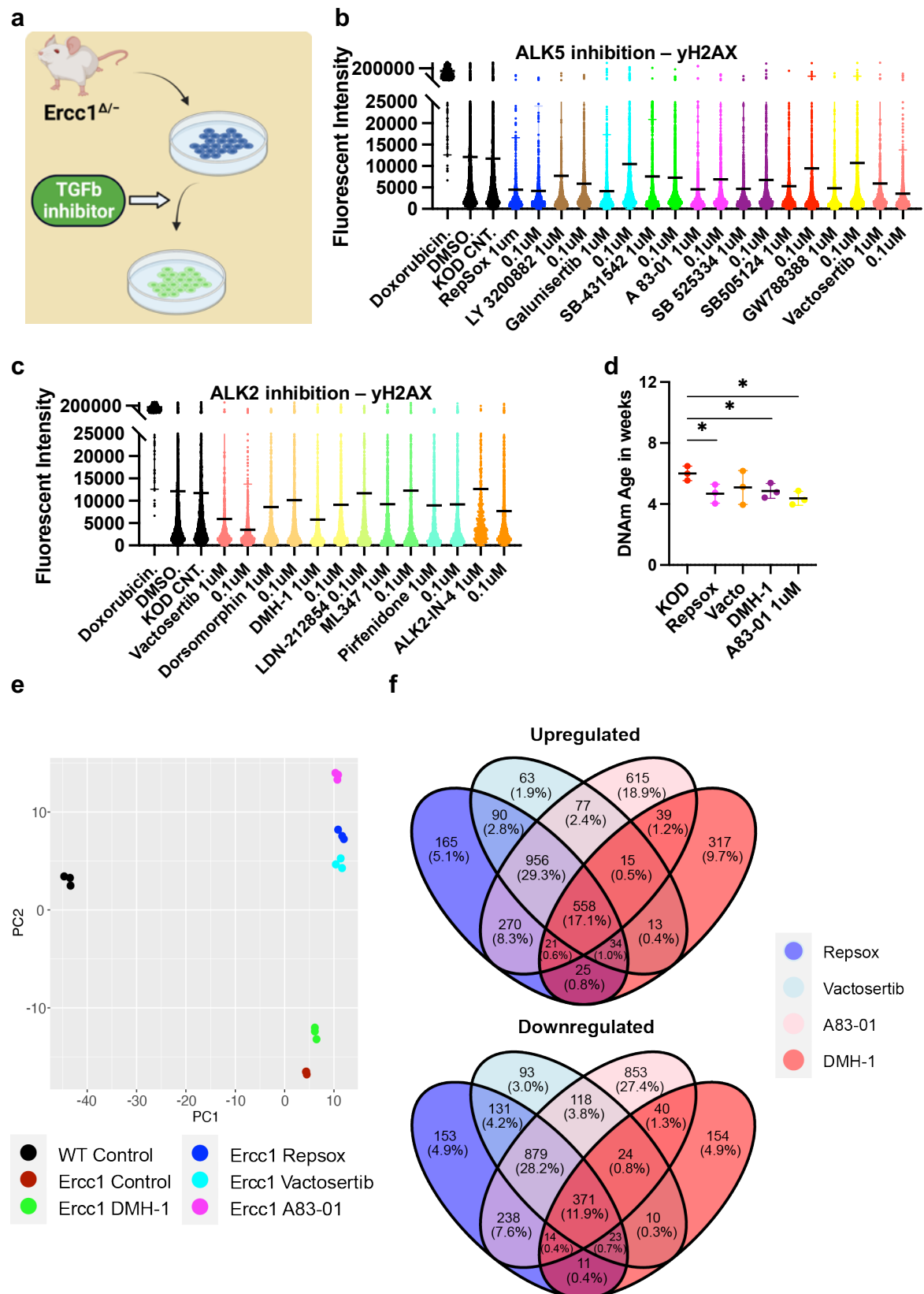
Fig. 4

Figure 4: Inhibition of ALK5 or ALK2 receptors improves DNA damage phenotype and resets the DNA methylation clock and transcriptome in Ercc1$^{\Delta/-}$
(a) Illustration of TGFb inhibitor screen on D/KO Fbs. **(b)** IF quantification of yH2AX mean levels in D/KO Fbs following treatment with ALK5 inhibitors, plated in 96 wells in triplicate and imaged with laser confocal at 40x. **(c)** IF quantification of yH2AX mean levels in D/KO Fbs following treatment with ALK 2 inhibitors, plated in 96 wells in triplicate. **(d)** DNA methylation clock (DNA Methylation Age Skin Final clock) analysis, comparing Repsox (0.1 um), Vactosertib (0.1 um), DMH-1 (1.0 um), and A83-01 (1.0 um) on D/KO Fbs, n = 3, * p<0.05 according to unpaired t-test. **(e)** Principal component analysis (PCA) of Ercc1 cells treated with TGFb inhibitors. Principal components 1 and 2 are shown. **(f)** Venn Diagram showing the overlap of significant genes (adjusted p-value < 0.05) for the TGFb inhibitors.
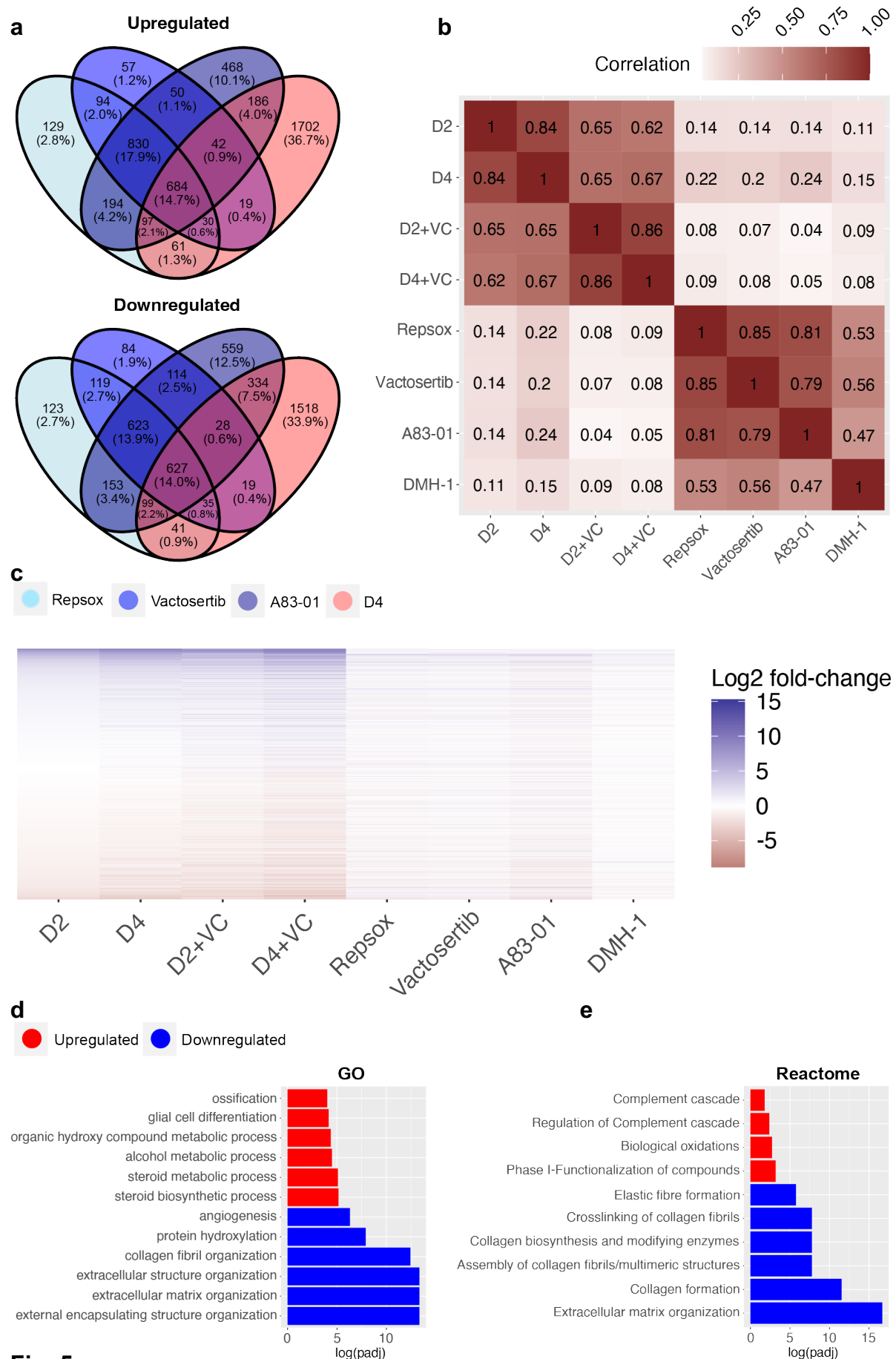
a

Upregulated

Downregulated

b

c

Repsox   Vactosertib   A83-01   D4

d   GO

Upregulated   Downregulated

ossification
glial cell differentiation
organic hydroxy compound metabolic process
alcohol metabolic process
steroid metabolic process
steroid biosynthetic process
angiogenesis
protein hydroxylation
collagen fibril organization
extracellular structure organization
extracellular matrix organization
external encapsulating structure organization

log(padj)

e   Reactome

Complement cascade
Regulation of Complement cascade
Biological oxidations
Phase I-Functionalization of compounds
Elastic fibre formation
Crosslinking of collagen fibrils
Collagen biosynthesis and modifying enzymes
Assembly of collagen fibrils/multimeric structures
Collagen formation
Extracellular matrix organization

log(padj)

Fig. 5

Figure 5: Transcriptomic comparison of Initation phase reprogramming with TGFb inhibition in Ercc1$^{\Delta/-}$. **(a)** Venn Diagram showing the overlap of significant genes (adjusted p-value < 0.05) for ALK5 inhibitors and 4 days of reprogramming. **(b)** Pairwise correlation between the log2 fold-changes of the filtered gene set (n=16883) of Ercc1 reprogramming and ALK5 or ALK2 inhibitors. **(c)** Heat map comparing Ercc1 reprogramming with TGFb inhibitors. Genes with a p-value lower than 1e-10 in at least one condition are shown. **(d and e)** GO and Reactome analysis of the intersect of significant genes as evaluated in 5A. Terms with the top six upregulated (red) and downregulated (blue) assessed by log(adjusted p-value) are shown.
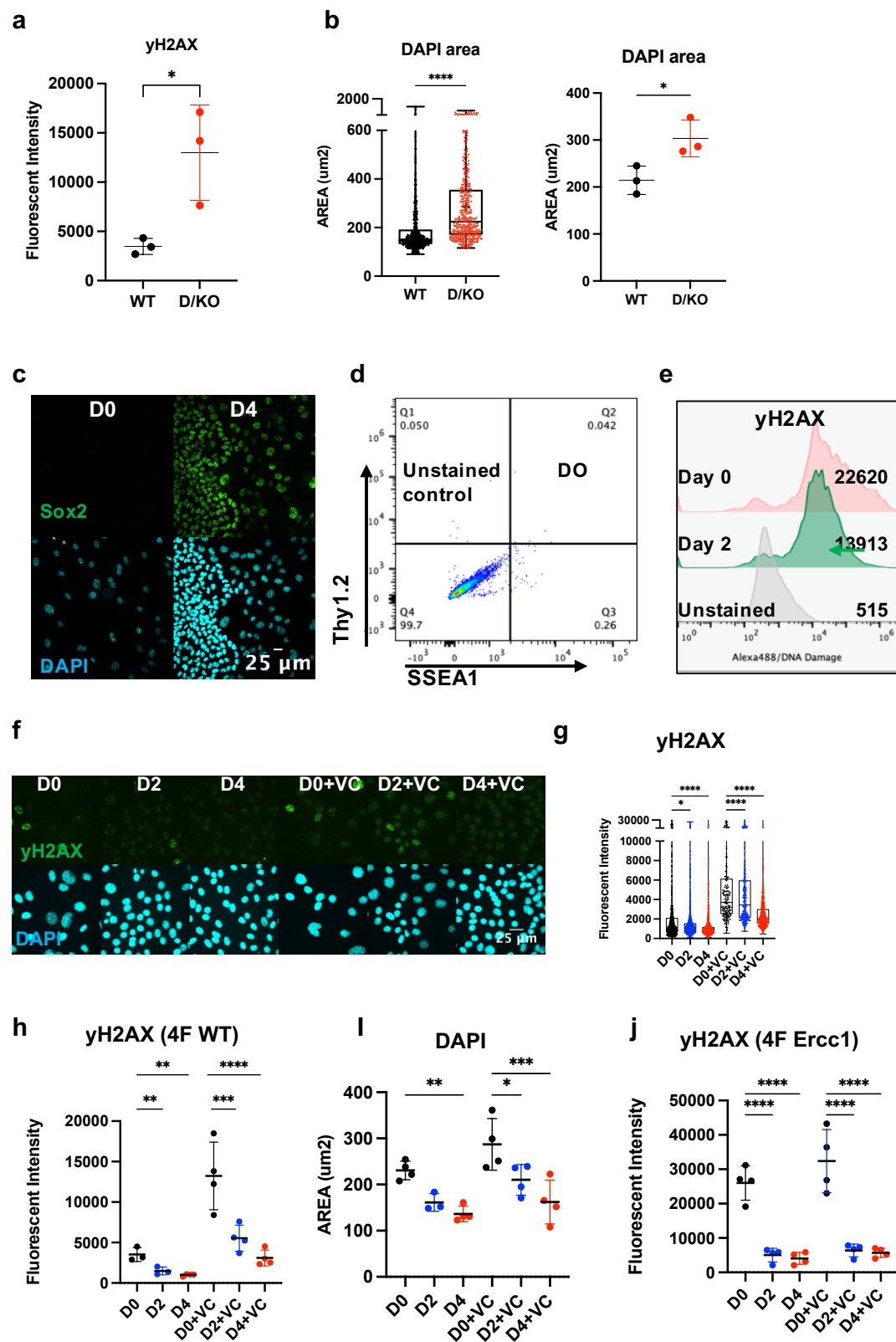
Fig. S1

Figure S1: Initiation phase reprogramming in 4Fj$^{+/-}$ rtTA$^{+/-}$ Ercc1$^{\Delta/-}$ accelerated aging model promotes DNA damage repair.

(a) Quantification of yH2AX IF from 3 experiments in fibroblasts from wildtype (WT) and Ercc1$^{\Delta/-}$ (D/KO) mice, imaged with Nikon laser confocal spinning disc, according to unpaired t-test, * $p<0.05$. **(b)**. Quantification of DAPI in fibroblasts from wildtype (WT) and Ercc1$^{\Delta/-}$ (D/KO) mice, imaged with Nikon laser confocal spinning disc, according to Mann-Whitney test, **** $p<0.0001$. Quantification of DAPI area from 3 experiments in fibroblasts from wildtype (WT) and Ercc1$^{\Delta/-}$ (D/KO) mice, imaged with Nikon laser confocal spinning disc, according to unpaired t-test, * $p<0.05$ **(c)** IF image of Sox2 and DAPI in 4F.D/KO Fbs after 4 days doxycycline induction, 40x **(d)** FACS unstained control for analysis of reprogramming Fbs markers Thy1.2 and SSEA1. **(e)** FACS analysis yH2AX levels following reprogramming of 4F.D/KO Fbs at day 0, day 2, and unstained control. **(f)** IF images of yH2AX and DAPI during representative time course analysis of 4F.WT Fb +/-VC at 100x. **(g)** Quantification of yH2AX images during time course shows significantly decreased levels at day 2 and day 4 according to one way ANOVA, **** $p<0.0001$. **(h)** Quantification of mean yH2AX levels in 4F WT from 3 or 4 experiments during time course shows significant decrease to levels at day 2 and day 4 according to one way ANOVA, ** $p<0.01$. **(i)** Quantification of DAPI area during time course shows decrease in size at day 2 and day 4 based on mean values of 4 experiments according to one way ANOVA, *** $p<0.001$, ** $p<0.01$, *$p<0.05$. **(j)** Quantification of mean yH2AX levels in 4F D/KO from 4 experiments during time course shows significant decrease to levels at day 2 and day 4 according to one way ANOVA, ** $p<0.0001$.
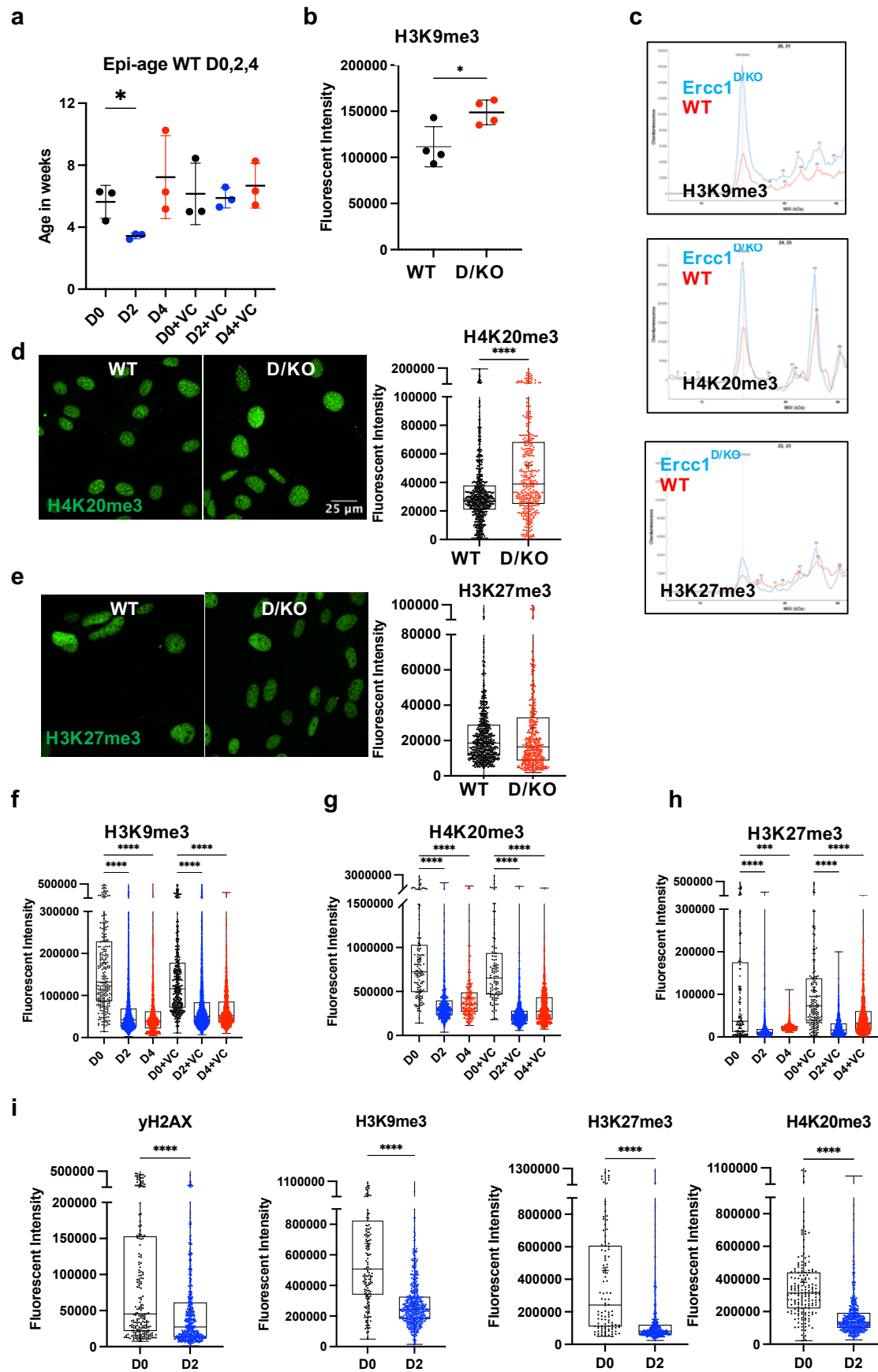
Fig. S2

Figure S2: DNA methylation clock is restored in Ercc1$^{\Delta/-}$ following short term reprogramming.
(a) DNA Methylation Age Skin Final clock analysis of WT Fb during time course, n = 3, * p<0.05 according to unpaired t-test. **(b)** Quantification of mean values of H3K9me3 levels in fibroblasts from WT and D/KO mice (n=4) according to unpaired t-test, * p<0.05. (**c**) Western capillary chemiluminescence quantification shows increased H3K9me3 and H4K20me3, with unchanged H3K27me3 in fibroblasts from D/KO vs WT mice (n=1 each). **(d)** IF and quantification shows increased H4K20me3 in fibroblasts from D/KO mice vs WT, imaged with Nikon laser confocal spinning disc, according to Mann-Whitney test, **** p<0.0001 **(e)** IF quantification shows unchaged H3K27me3 in fibroblasts from WT and D/KO mice, imaged with Nikon laser confocal spinning disc. **(f, g,h)** IF quantification of 2nd experiment shows significantly decreased H3K9me3, H4K20me3, and H3K27me3 levels during time course in 4F.D/KO Fbs after 2 and 4 days doxycycline induction with or without VC at 100x according to Kruskal-Wallis test, * p<0.000. **(i)** IF quantification of 3rd experiment shows yH2AX, H3K9me3, H4K20me3, and H3K27me3 in 4F.D/KO Fbs after 2 doxycycline induction at 100x according to Mann-Whitney test, * p<0.000.
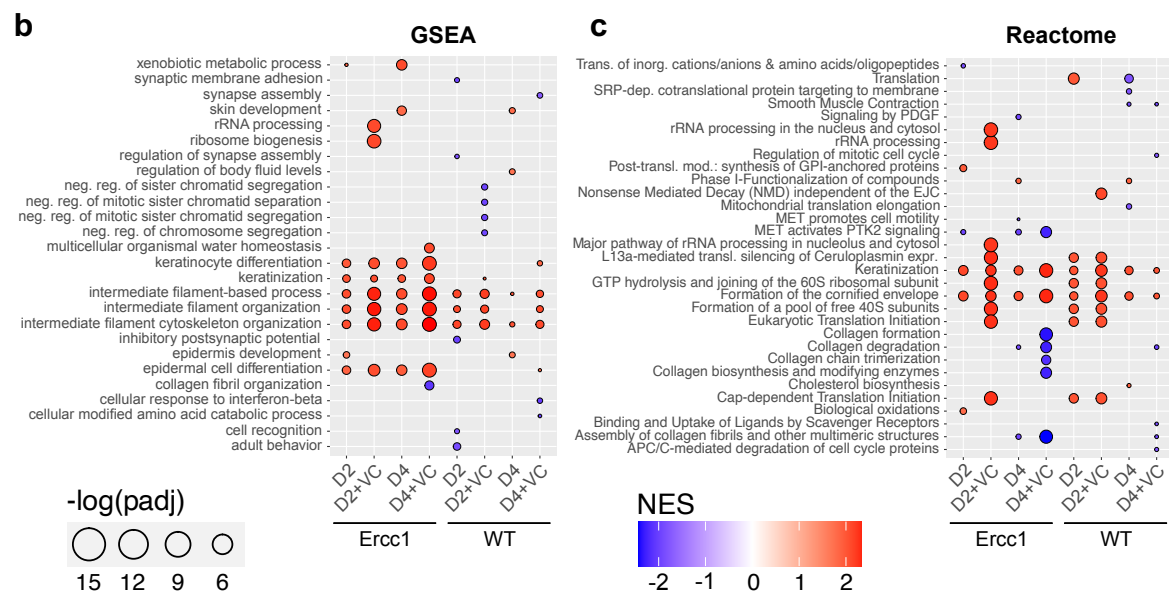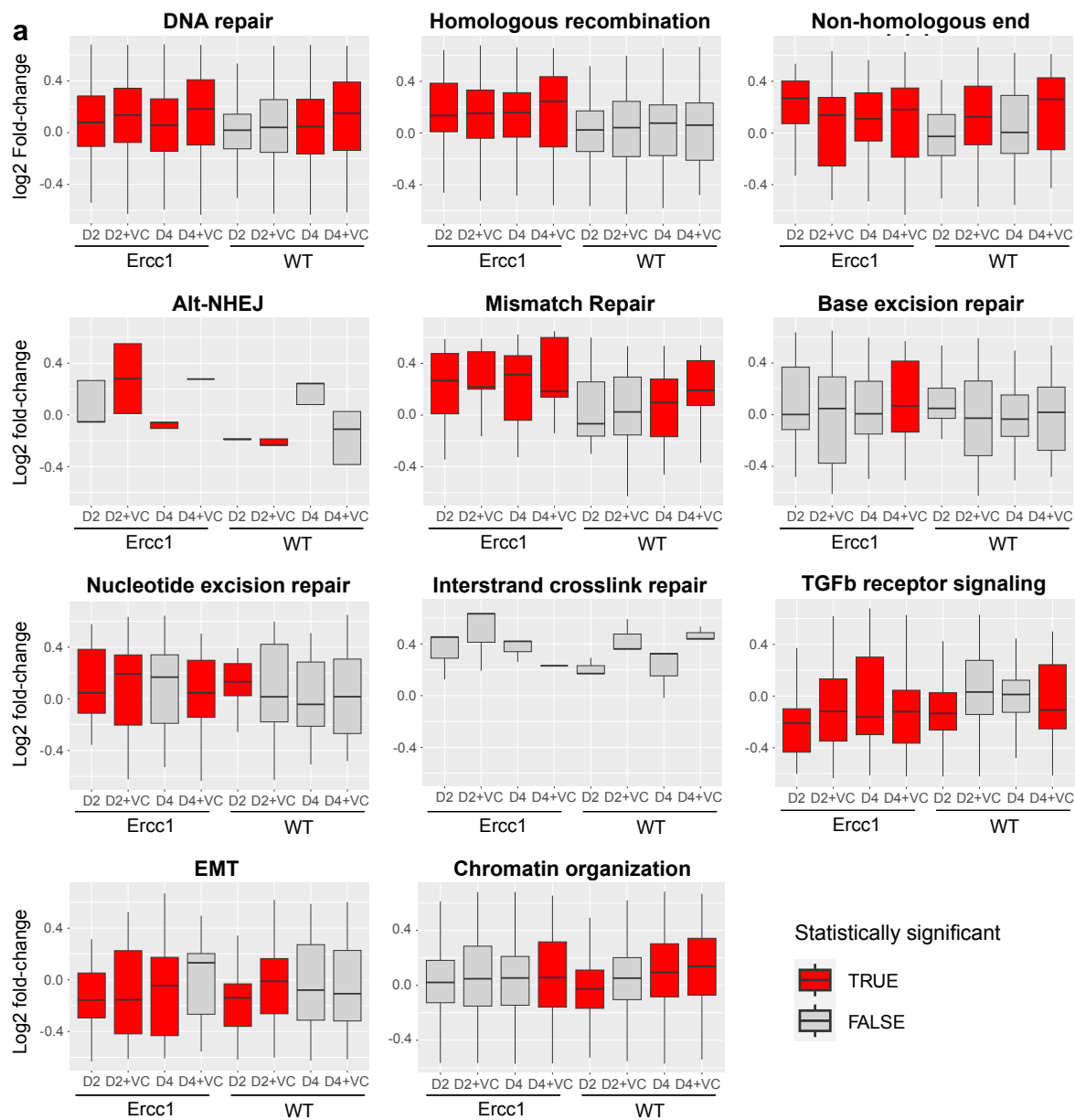
Fig. S3

Figure S3: Initation phase reprogramming drives transcriptomic reset and upregulates DNA repair and chromatin organization in Ercc1$^{\Delta/-}$
(a) Log2 fold-change of genes within a given GO pathway for Ercc1 and WT reprogramming at days 0, 2, and 4 with and without VC enhancement. The inner boxplot depicts medians and the first and third quartiles, with whiskers extending up to the 1.5x interquartile range and outliers removed for improved visualization of differences between conditions. Statistical significance (Wilcoxon Test, p-value < 0.05) is indicated by red coloring. **(b and c)** GSEA and Reactome analysis of Ercc1 and WT reprogramming considering log2 fold-changes between day 0 and day 2 of reprogramming and day 0 and day 4 of reprogramming with and without VC enhancement. Gene ontology biological process terms and Reactome terms are plotted against the normalized enrichment score (NES) with -log(adjusted p-value) illustrated through circle size. The top 10 terms for each condition are included.

a Dose titration for 15 TGFb inhibitors 0.1, 1, and 10 um

b

yH2AX

DAPI area

c yH2AX
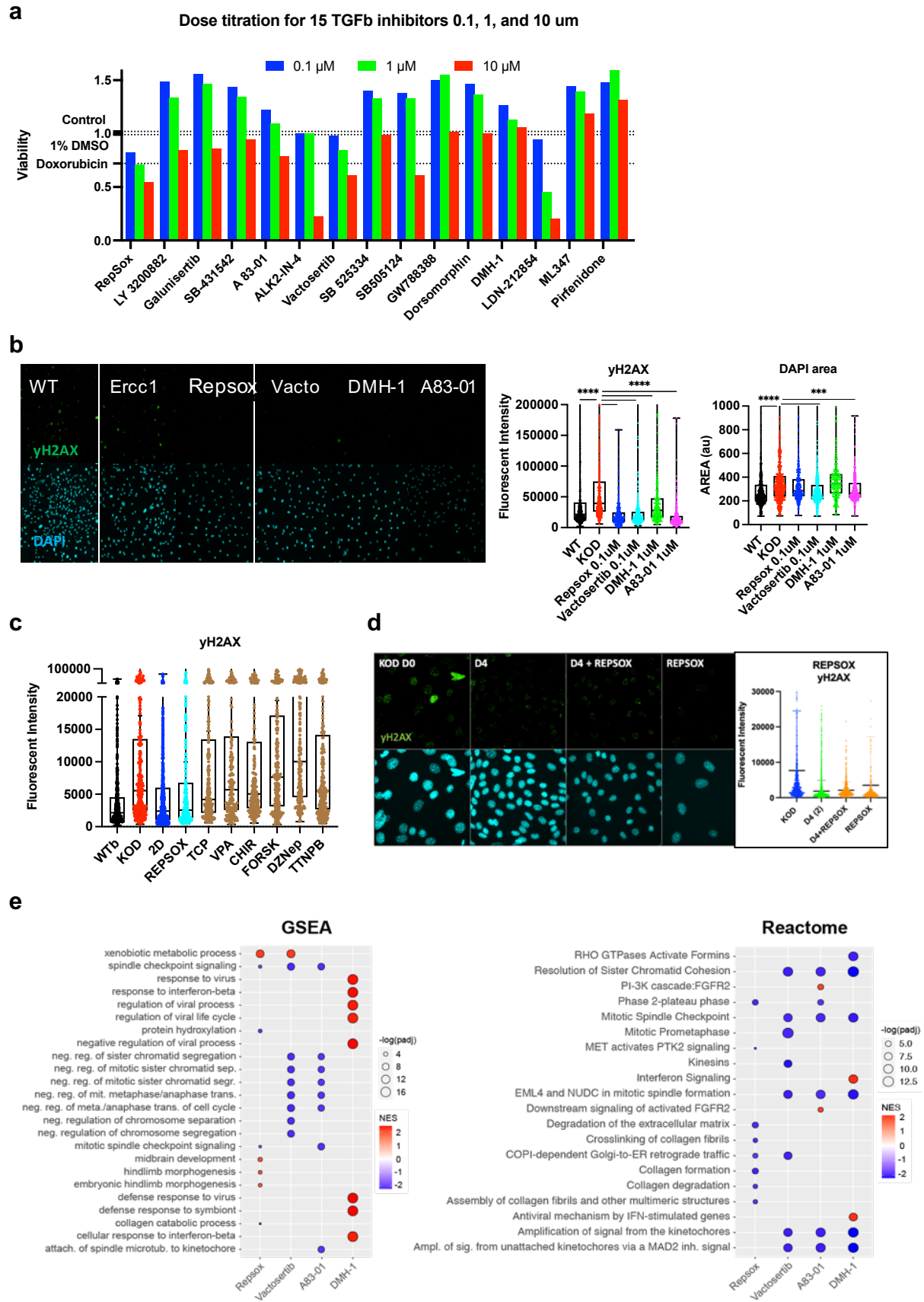
d

REPSOX yH2AX

e GSEA

Reactome

Fig. S4

Figure S4: Inhibition of ALK5 or ALK2 receptors improves DNA damage phenotype and resets the DNA methylation clock and transcriptome in Ercc1$^{\Delta/-}$
(a) Cell viability quantification using MTS assay in 96 well plates following treatment with high, medium, and low concentrations of 15 inhibitors in triplicate. Dosage range is 10um, 1um, and 0.1 um. Controls are represented by dashed lines and include untreated D/KO Fbs, 1% DMSO, and Doxorubicin (0.1um). **(b)** IF images and quantification of yH2AX levels and DAPI area in WT vs D/KO Fbs treated with Repsox, Vactosertib, DMH-1, and A83-01 in 24 wells plates, n = 1. **(c)** IF quantification of yH2AX levels comparing 2 days of doxycline induction to seven single small molecules used in chemical reprogramming at published dosages: Repsox (3um), TCP (10um), VPA (500um), CHIR99021 (5um), Forskolin (10um), DZNep (0.5um), and TTNPB (1um), n = 1. **(d)** IF images and quantification of yH2AX levels in 4F.D/KO cells after 4 days of induction either with doxycycline alone, doxycycline and Repsox, or Repsox alone, n = 1. **(e)** GSEA and Reactome analysis of Ercc1 cells treated with TGFb inhibitors considering log2 fold-changes, n = 3. Gene ontology biological process terms or Reactome terms are plotted against the normalized enrichment score (NES) with -log(adjusted p-value) indicated through circle size. The top 10 terms for each condition are included.
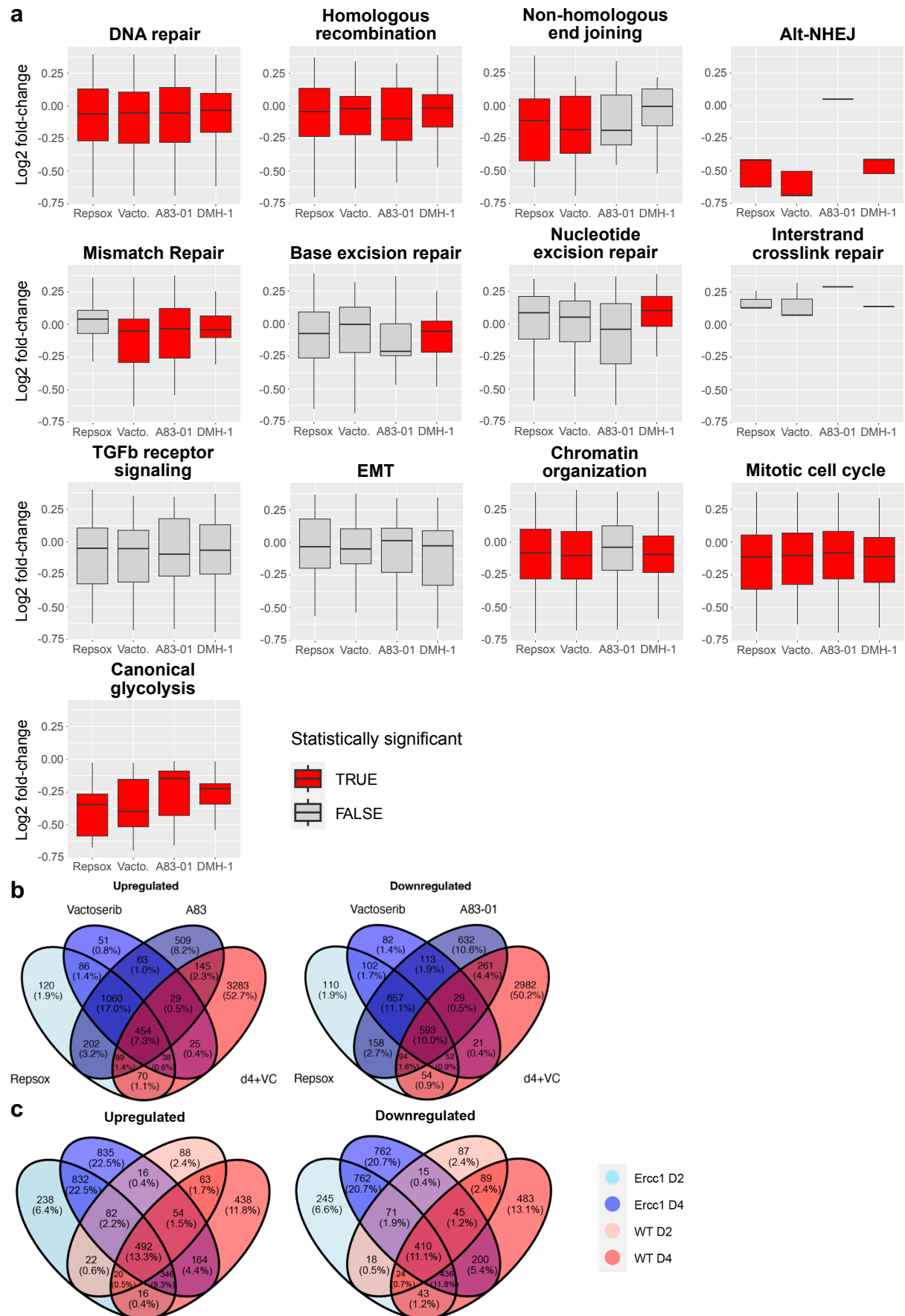
Fig. S5

Figure S5: GO term analysis of TGFb inhibition in Ercc1$^{\Delta/-}$. (a) Log2 fold-change of genes within a given GO pathway for Ercc1 cells treated with TGFb inhibitors compared to non-treated Ercc1 cells. The inner boxplot depicts medians and the first and third quartiles, with whiskers extending up to the 1.5x interquartile range and outliers removed for improved visualization of differences between conditions. Statistical significance (Wilcoxon Test, p-value < 0.05) is indicated by red coloring.
(b) Venn Diagram showing the overlap of significant genes (adjusted p-value < 0.05) for the ALK5 inhibitors and enhanced reprogramming day 4+VC. **(c)** Venn Diagram showing the overlap of significant genes (adjusted p-value < 0.05) for the reprogramming time course at day 2 and 4 without VC.